Geochimica et Cosmochimica Acta, Vol. 69, No. 2, pp. 225–257, 2005
Copyright © 2005 Elsevier Ltd
Printed in the USA. All rights reserved
0016-7037/05 $30.00 + .00

doi:10.1016/j.gca.2004.05.040

Prediction of surface charge on oxides in salt solutions: Revisions for 1:1 (M^+L^-) electrolytes

Dimitri A. Sverjensky*
Department of Earth and Planetary Sciences, The Johns Hopkins University, Baltimore, MD 21218, USA

(*Received July* 31, 2003; *accepted in revised form May* 25, 2004)

Abstract—Quantitative characterization of the development of proton surface charge on the surfaces of minerals is necessary for a fundamental understanding of reactions between minerals and aqueous electrolyte solutions. Despite many experimental studies of charge development, few attempts have been made to integrate the results of such studies with a theoretical framework that permits prediction. The present study builds on a theoretical framework to analyze a total of 55 sets of proton surface charge data referring to wide ranges of ionic strengths, and types of electrolyte and oxide. The resulting parameters were interpreted with the aid of crystal chemical, electrostatic, and thermodynamic theory, which enable a number of generalizations. Prediction of values of the pH_{ZPC} and ΔpK_n^θ reduces the number of triple-layer parameters to be estimated. New standard states for the equilibrium constants for electrolyte adsorption ($K_{M^+}^\theta$ and $K_{L^-}^\theta$) permit direct comparison of samples with a range of surface areas or site densities. Predicted cation binding on high dielectric constant solids (e.g., rutile) shows $K_{M^+}^\theta$, increasing in the sequence Cs^+, Rb^+, K^+, Na^+, Li^+. In contrast, on low dielectric constant solids (e.g., amorphous silica), the predicted sequence is Li^+, Na^+, K^+, Rb^+, Cs^+. The opposite sequences are attributable to the large solvation energy contribution opposing adsorption on low-dielectric constant solids. Cation and anion binding constants are in general different, which enables direct prediction of the point-of-zero-salt effect (pH_{PZSE}) relative to the pristine point-of-zero charge. The inner and outer capacitances in the triple-layer model (C_1 and C_2) are predictable parameters consistent with physically reasonable distances and interfacial dielectric constants for water. In summary, all the parameters in the triple-layer model can be estimated with the revised equations of this study, which enables prediction of proton surface charge for any oxide in 1:1 electrolyte solutions independent of experiments. Such predictions can serve as a complement to the experimental study of new oxide/electrolyte systems, or more complex systems, where additional mechanisms of charge development are likely. *Copyright © 2005 Elsevier Ltd*

1. INTRODUCTION

Many geochemical processes such as weathering, changes in the compositions of soils and groundwaters, scavenging of metals in the ocean, the chemical evolution of shallow ore-forming fluids, and the fate of contaminants in groundwaters, involve adsorption phenomena at the mineral–water interface (Parks, 1975; Skinner, 1979; Sposito, 1984; Davis and Kent, 1990; Stumm, 1992; Drever, 1997; Langmuir, 1997). Adsorption on mineral surfaces of protons, metallic cations, anions, and organic species can all contribute to, and are influenced by, the development of surface charge. Consequently, a quantitative characterization of surface charge on minerals is necessary for a fundamental understanding of geochemical processes. On oxide minerals, the principal mechanism of the development of surface charge is the adsorption of protons, hydroxyls, and electrolyte cations and anions—termed proton surface charge (James and Parks, 1982; Davis and Kent, 1990). On silicate, carbonate and other mineral surfaces, additional mechanisms of surface charge development are probably at least as important as proton surface charge. Considerable effort has been focussed on an understanding of proton surface charge development on oxide surfaces.

Quantitative modeling of proton surface charge on oxides and hydroxides has progressed through the development of surface complexation models linking surface chemistry and aqueous chemistry (summarized in James and Parks, 1982; Sposito, 1984; Hunter, 1986, 1989; Schindler and Stumm, 1987; Hiemstra et al., 1989a,b, 1990; Hiemstra and van Riemsdijk, 1996; Davis and Kent, 1990; Dzombak and Morel, 1990; Stumm, 1992; Rudzinski et al., 1991, 1992, 1993, 1998, 2000; Rustad et al., 1996a,b; Robertson and Leckie, 1997; Felmy and Rustad, 1998). The applicability of surface complexation models to more complex minerals such as silicates would be greatly facilitated if the available results for oxides could be used as a basis for the prediction of the development of proton surface charge on silicates. Similarly, the applicability of surface complexation models to natural systems would be enhanced by the availability of sets of consistent surface equilibrium constants applicable to wide ranges of ionic strength and different electrolyte types. In this regard, the 1:1 electrolyte solution most often used in experiments, e.g., $NaNO_3$, differs from the compositions of shallow groundwaters dominated by dilute Ca-Na-HCO_3-SiO_2 species (Drever, 1997). Consequently, effective surface equilibrium constants referring specifically to $NaNO_3$ or similar electrolyte solutions are not relevent to most natural groundwaters. It can be imagined that a very large number of experimentally derived equilibrium constants would be needed to characterize the surface complexation of protons and electrolyte ions to all the geochemically important minerals over a wide range of aqueous solution compositions, temperatures,

* Author to whom correspondence should be addressed (sver@jhu.edu).

and pressures. Under these circumstances, a theoretical basis for predicting such surface-complexation equilibrium constants would be extremely useful.

Prediction of proton surface charge has received considerable attention using a variety of methods. In the context of multisite models of oxide surfaces, electrostatic bonding theory (Hiemstra et al., 1989a,b; Hiemstra and van Riemsdijk, 1996) has been used to estimate the surface protonation equilibrium constants of sites on different crystal planes on oxides and hydroxides. Refinement of this method has been developed and applied in numerous studies. However, in many applications of the CD-MUSIC model, a single numerical value for the surface protonation equilibrium constants of the different sites has been employed (Hiemstra and van Riemsdijk, 1996; Venema et al., 1996, 1997; Geelhoed et al., 1997; Hiemstra and Van Riemsdijk, 2000; Bourikas et al., 2001). This effectively results in a single-site model with respect to surface protonation and electrolyte adsorption (although the model is still a 1-pK model). This situation is analogous to the application of the 2-site model of Dzombak and Morel (1990), where the same surface protonation equilibrium constants are used for the strong and the weak sites. When surface complexation models are only used for proton surface charge data, a single-site model with respect to surface protonation and electrolyte adsorption is the most practical choice. However, surface site heterogeneity may play a greater role when a variety of surface measurements, such as electrokinetic and calorimetric studies are also taken into consideration (Rudzinski et al., 1991, 1992, 1993, 1998).

Prediction of surface protonation on oxides and hydroxides taking into account different sites on different crystal planes has also been addressed by combining molecular dynamics methods with linear free energy correlations (Rustad et al., 1996a,b; Felmy and Rustad, 1998). Here too it was necessary to include the adsorption of electrolyte ions which contribute substantially to the development of proton surface charge. Ultimately, the applications of all multisite approaches are hampered by the lack of experimental data for proton surface charge on single crystal surfaces. Until such data become available, it is not possible to directly test predictions of surface protonation on different crystal surfaces.

The approach used in the present study builds on the single-site triple-layer model and crystal chemical and Born solvation theory. As described previously (Sverjensky and Sahai, 1996; Sahai and Sverjensky, 1997a; Sahai and Sverjensky, 1997b; Koretsky et al., 1998) this approach results in a predictive model for proton surface charge development. A single-site surface complexation model is used because all the available proton surface charge data on oxides refer to powders immersed in salt solutions. The data consequently consist of an averaging over many crystal planes and different sites. Such averaging is conveniently treated with a single-site model. Furthermore, as new experimental data on powders are obtained, they serve as a test of the model predictions. The triple-layer model is used here because it has a level of complexity required to account for a range of electrolyte types and concentrations. As before, the approach adopted involves two steps. First, many experimental studies of proton surface charge data for oxides and hydroxides referring to wide ranges of ionic strengths and electrolyte types are analyzed. Second, the results of this analysis are interpreted and correlated with the aid of crystal chemical, electrostatic, and thermodynamic theory. In this way, all the necessary parameters for prediction of proton surface charge, including site densities, surface protonation and electrolyte adsorption equilibrium constants and capacitances can be placed on a predictive basis. The purpose of developing an extended triple-layer model (ETLM) with crystal-chemical and electrostatic theory is that predictions can be made for electrolytes and solids that have not been investigated experimentally.

Recent advances in the definition and interpretation of standard states for the thermodynamic activities of surface sites and species facilitate a more accurate comparison of the equilibrium constants for surface protonation and electrolyte adsorption for different samples of the same solid, as well as for samples of different solids. In the present study, attention is focussed on developing a revised ETLM consistent with the new standard states. The many proton surface charge data sets analyzed previously (Criscenti and Sverjensky, 1999; Sahai and Sverjensky, 1997a; Sverjensky, 2001) are supplemented by additional data regressed in the present study (Appendix). These data considerably expand the number of data sets previously analyzed, particularly for goethite, hematite, and amorphous silica. As a result, revised predictive correlations for protonation, electrolyte adsorption, and capacitances are presented below.

2. SUMMARY OF THEORETICAL RELATIONS

2.1. Surface Protonation

2.1.1. Thermodynamic Relations

The surface protonation equilibrium constants corresponding to the equilibria

$$>SOH + H^+ = >SOH_2^+ \quad (1)$$

$$>SO^- + H^+ = >SOH \quad (2)$$

can be written

$$K_1^\theta = \frac{a_{>SOH_2^+}}{a_{>SOH} a_{H^+}} 10^{\frac{F\psi_0}{2.303RT}} \quad (3)$$

and

$$K_2^\theta = \frac{a_{>SOH}}{a_{>SO^-} a_{H^+}} 10^{\frac{F\psi_0}{2.303RT}} \quad (4)$$

where the superscript "θ" represents the standard states for sorbent sites ($>SOH$) and sorbate species ($>SOH_2^+$, $>SO^-$, Sverjensky, 2003), $a_{>SOH_2^+}$, $a_{>SO^-}$, $a_{>SOH}$, and a_{H^+} represent thermodynamic activities, ψ_0 represents the potential (V) at the 0-plane of the triple-layer model where H^+ and OH^- adsorb, F = 96,485 C · mole^{-1}, and R and T represent the universal gas constant and temperature (K), respectively. For the sorbent sites, the standard state refers to unit activity of surface sorption sites on a completely unsaturated surface at any P and T and

$$a_{>SOH} = \lambda_{>SOH} X_{>SOH} \quad (5)$$

where $\lambda_{>SOH} \rightarrow 1$ *as* $X_{>SOH} \rightarrow 1$ (i.e. a hypothetical standard state). For the sorbate species, the standard state refers to unit

activity of surface species on a completely saturated surface with zero potential at any P and T referenced to infinite dilution, expressed by

$$a_{>SOH_2^+} = \lambda_{>SOH_2^+} X_{>SOH_2^+} \tag{6}$$

where $\lambda_{>SOH_2^+} \to 1$ and $\psi_0 \to 0$ as $X_{>SOH_2^+} \to 0$ (i.e. a hypothetical standard state). An advantage of defining the standard states for sorption sites and sorbate species in this way is that in model calculations the limiting conditions of $X_{>SOH} \to 1$ and $X_{>SOH_2^+} \to 0$ are often approached. In other words, for the triple-layer model used here, $>SOH$ is commonly by far the dominant species, whereas sorbates such as $>SOH_2^+$ are minor species. Under these circumstances, it is reasonable to assume that $\lambda_{>SOH} \approx 1$ and $\lambda_{>SOH_2^+} \approx 1$ (for an alternate approach, where activity coefficient corrections are developed, see Kulik, 2000, 2002).

The equilibrium constants K_1^θ and K_2^θ are related to those for the equilibria

$$>SO^- + 2H^+ = >SOH_2^+ \tag{7}$$

and

$$>SO^- + >SOH_2^+ = 2>SOH \tag{8}$$

by

$$K_1^\theta K_2^\theta = K_{ZPC}^\theta = \frac{a_{>SOH_2^+}}{a_{>SO^-}(a_{H^+})^2} \tag{9}$$

and

$$\frac{K_2^\theta}{K_1^\theta} = K_n^\theta = \frac{(a_{>SOH})^2}{a_{>SOH_2^+} a_{>SO^-}} \tag{10}$$

respectively.

In practice, values of $\log K_1^\theta$ and $\log K_2^\theta$ are calculated from

$$\log K_1^\theta = pH_{ZPC} - \frac{\Delta pK_n^\theta}{2} \tag{11}$$

and

$$\log K_2^\theta = pH_{ZPC} + \frac{\Delta pK_n^\theta}{2} \tag{12}$$

where

$$pH_{ZPC} = \frac{\log K_{ZPC}^\theta}{2} \tag{13}$$

$$\Delta pK_n^\theta = \log K_n^\theta \tag{14}$$

Values of pH_{ZPC} can be obtained experimentally, and predicted using solvation and crystal chemical theory (Sverjensky and Sahai, 1996; see below). Similarly, values of ΔpK_n^θ can be derived by analysis of experimental surface protonation data (with the assumption of a site density), and predicted using crystal chemical theory (Sverjensky and Sahai, 1996; see also below).

The new standard states adopted above are related to the widely used hypothetical 1.0 M standard state (Sverjensky, 2003) by

$$K_1^\theta = K_1^0 \left(\frac{N_s A_s}{N^\ddagger A^\ddagger} \right) \tag{15}$$

$$K_2^\theta = K_2^0 \left(\frac{N_s A_s}{N^\ddagger A^\ddagger} \right)^{-1} \tag{16}$$

$$K_{ZPC}^\theta = K_{ZPC}^0 \tag{17}$$

and

$$K_n^\theta = K_n^0 \left(\frac{N_s A_s}{N^\ddagger A^\ddagger} \right)^{-2} \tag{18}$$

where the superscript "0" represents the hypothetical 1.0 M standard state, N_s represents the surface site density on the sth solid sorbent (sites $\cdot$ m^{-2}), $N^\ddagger$ represents the standard state sorbate species site density (sites $\cdot$ m^{-2}), A_s represents the BET surface area of the sth solid sorbent (m$^2 \cdot$ g^{-1}), and $A^\ddagger$ represents a standard state BET surface area (m$^2 \cdot$ g^{-1}). In the present study, values of $N^\ddagger = 10 \times 10^{18}$ sites $\cdot$ m^{-2} and $A^\ddagger =$ 10 m$^2 \cdot$ g^{-1} are selected for all solids. It is emphasized that these values are properties of the hypothetical standard state (for sorbates) applicable to all samples of all solids.

2.1.2. *Predictive Equations Based on Crystal Chemistry and Solvation Theory*

It has been previously proposed (Sverjensky and Sahai, 1996) that the standard Gibbs free energy of the νth surface protonation reaction ($\Delta G_{r,\nu}^0$) can be broken up into three terms according to

$$\Delta G_{r,\nu}^0 = \Delta G_{s,\nu}^0 + \Delta G_{pi,\nu}^0 + \Delta G_{ii,\nu}^0 \tag{19}$$

where $\Delta G_{s,\nu}^0$ represents a Born solvation contribution, $\Delta G_{pi,\nu}^0$ represents an electrostatic proton interaction term, and $\Delta G_{ii,\nu}^0$ represents a term intrinsic to the aqueous proton. The Born solvation term is treated by building on earlier studies of metal adsorption (James and Healy, 1972). The proton interaction term is built by summing an attractive interaction between the proton and the surface oxygen with a repulsive interaction between the proton and the underlying metal of the solid sorbent (Yoon et al., 1979).

Predictive equations for the surface protonation equilibrium constants $\log K_{ZPC}$ and ΔpK_n^θ derived using the above approach (Sverjensky and Sahai, 1996) result in

$$\log K_{ZPC}^\theta = \frac{-\Delta\Omega_{r,ZPC}}{2.303RT}\left(\frac{1}{\varepsilon_s}\right) - B_{ZPC}\left(\frac{s}{r_{H^+}}\right) + \log K''_{ii,ZPC} \tag{20}$$

and

$$\Delta pK_n^\theta = -B_n\left(\frac{s}{r_{H^+}}\right) + \log K''_{ii,n} \tag{21}$$

where ε_s and $\dfrac{s}{r_{H^+}}$ are variables representing the dielectric constant and the Pauling bond strength per angstrom, respec-

Table 1. Bulk dielectric constants (ε_s[a]), interfacial dielectric constants ($\varepsilon_{int.,s}$[b]), and distance parameters $r_{1,s}$[b] and $r_{M^+,s}$[b] for Li^+, Na^+, K^+, Rb^+, Cs^+, NH_4^+, and $N(CH_3)_4^+$ on the sth solid oxide for use in predicting capacitances and equilibrium adsorption constants.

Solid	ε_s	$\varepsilon_{int.,s}$	$r_{1,s}$	$r_{Li^+,s}$	$r_{Na^+,s}$	$r_{K^+,s}$	$r_{Rb^+,s}$	$r_{Cs^+,s}$	$r_{NH_4^+,s}$	$r_{N(CH_3)_4^+,s}$
Fe_3O_4	1000[c]	26	0.75	0.74	1.02	1.38	1.49	1.70	1.47	3.47
α-MnO_2	1000[c]	26	0.75	0.74	1.02	1.38	1.49	1.70	1.47	3.47
α-TiO_2	121	26	0.75	0.74	1.02	1.38	1.49	1.70	1.47	3.47
β-TiO_2	18.6[c]	26	0.75	0.74	1.02	1.38	1.49	1.70	1.47	3.47
FeOOH	15[c]			2.37	1.83	1.38	1.49	1.70	1.47	3.47
Fe_2O_3[d]	12[c]	53	3.5	2.37	1.83	1.38	1.49	1.70	1.47	3.47
Fe_2O_3[e]	12[c]	22[h]	0.7[h]	0.74	1.02	1.38	1.49	1.70	1.47	3.47
α-Al_2O_3	10.4	53	2.9	2.37	1.83	1.38	1.49	1.70	1.47	3.47
γ-Al_2O_3	10.4	53	2.9	2.37	1.83	1.38	1.49	1.70	1.47	3.47
$Al(OH)_3$	8.4	32[h]	2.9[h]	2.37	1.83	1.38	1.49	1.70	1.47	3.47
α-SiO_2	4.6	43[h]	4.5[h]	2.37	1.83	1.38	1.49	1.70	1.47	3.47
am. SiO_2[f]	3.8[c]	43[h]	4.0[h]	2.37	1.83	1.38	1.49	1.70	1.47	3.47
am. SiO_2[g]	3.8[c]	43[h]	1.8[h]	2.37	1.83	1.38	1.49	1.70	1.47	3.47

[a] Dielectric constants from Shannon (1993) and Olhoeft (1981), except where otherwise indicated.
[b] From Sverjensky (2001) unless otherwise noted.
[c] Dielectric constant values for Fe_3O_4 and α-MnO_2 are minimum values, indicating that there are no Born solvation effects for these solids. The value for β-TiO_2 was calculated using the estimation procedure in Shannon et al. (1992). Values for amorphous silicas are assumed to be the same as for amorphous silica glass. Values for goethite and hematite were computed from pH(ZPC) values of 9.15 (Lumsden and Evans, 1994) and 9.5 (Christl and Kretzschmar, 1999), respectively using Eqn. 49.
[d] Hematites with pH_{ZPC} = 8.4–8.6.
[e] Hematites with pH_{ZPC} = 9.0–9.5 (intensively cleaned).
[f] DeGussa Aerosil amorphous silica.
[g] Amorphous silicas other than DeGussa.
[h] Present study (see text).

tively, for the sth solid. The term involving the dielectric constant of the solid in Eqn. (20) arises from the solvation term in Eqn. (19), whereas the terms involving the Pauling bond strength arise from the electrostatic interaction term in Eqn. (19). Values of ε_s and $\frac{s}{r_{H^+}}$ are known independently for a wide range of solids (Tables 1 and 2). The symbols $\Delta\Omega_{r,ZPC}$, B_{ZPC}, B_n, $\log K''_{ii,ZPC}$, and $\log K''_{ii,n}$ refer to coefficients obtained by calibration of the equations with experimentally derived equilibrium constants. It is this calibration that will be revised below.

Table 2. Pauling bond-strengths (s[a]), average metal–oxygen bond lengths in the bulk crystal structure (r_{M-O}[a]), and bond strengths per angstrom $\left(\frac{s}{r_{M^+}}\right)$[b] for adsorbed H^+, Li^+, Na^+, K^+, Rb^+, Cs^+, Ag^+, Tl^+, NH_4^+, and $N(CH_3)_4^+$ for use in predictive equations involving Born solvation and crystal chemical theory.

Solid	s	r_{M-O}	$\frac{s}{r_{H^+}}$	$\frac{s}{r_{Li^+}}$	$\frac{s}{r_{Na^+}}$	$\frac{s}{r_{K^+}}$	$\frac{s}{r_{Rb^+}}$	$\frac{s}{r_{Cs^+}}$	$\frac{s}{r_{Ag^+}}$	$\frac{s}{r_{Tl^+}}$	$\frac{s}{r_{NH_4^+}}$	$\frac{s}{r_{N(CH_3)_4^+}}$
Fe_3O_4	[c]	2.059	0.1768	0.117	0.109	0.0995	0.0969	0.0924	0.102	0.0967	0.0974	0.0664
α-MnO_2	0.6667	1.887	0.2301	0.197	0.182	0.166	0.162	0.154	0.171	0.161	0.162	0.109
α-TiO_2	0.6667	1.955	0.2248	0.194	0.179	0.163	0.159	0.151	0.168	0.159	0.160	0.108
β-TiO_2	0.6667	1.946	0.2299	0.194	0.179	0.164	0.159	0.152	0.169	0.159	0.160	0.108
FeOOH	0.5000	2.021	0.1650	0.0481	0.0508	0.0532	0.053	0.0514	0.0539	0.0525	0.0527	0.0435
Fe_2O_3[d]	0.5000	2.03	0.1645	0.0633	0.0679	0.0724	0.0712	0.0692	0.0736	0.0711	0.0714	0.0556
Fe_2O_3[e]	0.5000	2.03	0.1645	0.1441	0.133	0.122	0.110	0.105	0.125	0.118	0.110	0.0766
α-Al_2O_3	0.5000	1.913	0.1711	0.0696	0.0753	0.0807	0.0793	0.0768	0.0823	0.0792	0.0796	0.0604
γ-Al_2O_3		1.913	0.190[h]	0.0696	0.0753	0.0807	0.0793	0.0768	0.0823	0.0792	0.0796	0.0604
$Al(OH)_3$	0.5000	1.902	0.1716	0.0697	0.0754	0.0809	0.0795	0.0769	0.0825	0.0793	0.0796	0.0604
α-SiO_2	1.000	1.609	0.3818	0.118	0.126	0.134	0.132	0.128	0.136	0.147	0.132	0.104
am. SiO_2[f]	1.000	1.609	0.3818	0.125	0.134	0.143	0.141	0.137	0.146	0.141	0.141	0.110
am. SiO_2[g]	1.000	1.609	0.3818	0.173	0.191	0.209	0.204	0.196	0.214	0.204	0.205	0.145

[a] Values of s and r_{M-O} represent Pauling bond strengths and mean metal–oxygen interatomic distances (respectively) derived from Smyth and Bish (1988).
[b] Calculated using the tabulated values of s and r_{M-O} and Eqns. (44) and (46), except for $r_{H^+} = r_{M-O} + 1.01$ (Sverjensky and Sahai, 1996).
[c] For crystal structures with more than one kind of cation site an average for the whole structure was used: 0.4167 for octahedral sites and 0.75 for tetrahedral sites.
[d] Hematites with pH_{ZPC} = 8.4–8.6.
[e] Hematites with pH_{ZPC} = 9.0–9.5 (intensively cleaned).
[f] DeGussa Aerosil amorphous silica.
[g] Other amorphous silicas, including Cabosil.
[h] Calculated from the pH(ZPC) value of 8.6 (Table 5) using Eqn. (49).

Table 3. Regression slopes, intercepts, and B_M *or* B_L values from Figures 3 and 4, and predicted values of $\Delta\Omega_{r,j}$ and log $K''_{ii,j}$ for the adsorption of the jth monovalent cation or anion on oxide surfaces generated with Eqns. (58)–(62), (70)–(73), and (75) and the crystallographic radii (Å) and aqueous equilibrium constants listed.

Ion	Slopes	$\Delta\Omega_{r,j}$[a] expt.	Intcpts.	B_M *or* B_L	$r_{x,j}$[b]	log K_{aq}[c]	$\Delta\Omega_{r,j}$ pred.	Slopes pred.	log $K''_{ii,j}$ pred.
Li^+	−10.4	14.2	5.2	10	0.74	0.36	14.3	−10.5	5.3
Na^+	−7.37	10.0	4.4	8	1.02	−0.18	9.63	−7.1	4.3
K^+	−3.35	4.6	3.7	7	1.38	−0.46	5.46	−4.0	3.8
Rb^+			3.8[d]	7	1.49		4.63	−3.4	3.8
Cs^+	−1.75	2.4	3.5	5	1.70		2.79	−2.0	3.5
Ag^+			8.3[e]	7	1.26	2.0	6.68	−4.9	8.3
Tl^+				7	1.50	0.79	4.37	−3.2	6.1
NH_4^+				7	1.47	4.75[i]	4.63	−3.4	13.4
$N(CH_4)_3^+$	0.0		3.4	0	3.47[h]		0.0	0.0	3.4
F^-				2	1.33	3.17[i]	15.5	−11.4	6.9
Cl^-	−7.91	10.8	4.3	2	1.81	−0.71[j]	11.6	−8.5	4.3
Br^-			4.3[f]	2	1.95		10.7	−7.8	4.3
I^-			4.9[g]	2	2.2		9.41	−6.9	4.9
HS^-				2	1.84	6.99[i]	11.4	−8.4	9.4
OH^-				2	1.4	14.0	14.9	−10.9	13.9
NO_2^-				2	2.57	3.23	7.79	−5.7	6.9
NO_3^-	−5.37	7.3	3.9	2	2.97	−1.3[i]	6.41	−4.7	3.9
ClO_4^-			3.0[g]	2	3.85		4.22	−3.1	3.0

[a] Calculated from the given slopes and the first term of Eqns. (40) or (41).
[b] Crystallographic radii for cations refer to VI-fold coordination from Shannon and Prewitt (1969) unless otherwise stated. Crystallographic radii for anions equal to the effective electrostatic radii in Shock and Helgeson (1988).
[c] Equilibrium association constants corresponding to $M^+ + OH^- = MOH^0$ and $H^+ + L^- = HL^0$ taken from Baes and Mesmer (1976) and Shock et al. (1997), respectively (unless otherwise noted).
[d] Estimated using Eqn. (41) and $\log^*K^0_{Rb^+} = -6.2$ (based on evaluation of preliminary surface titration data for rutile in RbCl from Machesky et al., personal communication) and a predicted value of $\Delta\Omega_{r,Rb^+}$.
[e] Estimated using Eqn. (41) with a $\log^*K^0_{Ag^+}$ value from Davis and Leckie (1978) and a predicted value of $\Delta\Omega_{r,Ag^+}$.
[f] Assumed to be the same as for Cl^- based on surface titration data in Sprycha (1984).
[g] Estimated using Eqn. (41) with $\log^*K^0_{L^-}$ values from Table A1 and predicted values of $\Delta\Omega_{r,L^-}$.
[h] Estimated by Robinson and Stokes (1959; p. 122).
[i] Shock et al. (1989).
[j] Sverjensky et al. (1991).

The symbol $\Delta\Omega_{r,ZPC}$ in Eqn. (20) represents a Born solvation coefficient for the reaction given by

$$\Delta\Omega_{r,ZPC} = \Omega_{>SOH_2^+} - \Omega_{>SO^-} = \Omega^{abs.}_{>SOH_2^+} - \Omega^{abs.}_{>SO^-} \quad (22)$$

where $\Omega_{>SOH_2^+}$ and $\Omega_{>SO^-}$ represent conventional Born coefficients and $\Omega^{abs.}_{>SOH_2^+}$ and $\Omega^{abs.}_{>SO^-}$ represent absolute Born coefficients for the species $>SOH_2^+$ and $>SO^-$, analogous to the conventional and absolute Born coefficients for aqueous ions (Helgeson and Kirkham, 1976). The relationship between the conventional and absolute Born coefficients for the jth surface species is given by

$$\Omega^{abs.}_j = \Omega_j + \Omega^{abs.}_{>SOH} \quad (23)$$

which is based on the convention adopted here that

$$\Omega_{>SOH} = 0.0 \quad (24)$$

Definitions of absolute and conventional Born coefficients are necessary to provide a basis for relating experimentally accessible quantities to absolute solvation coefficients calculated with Born solvation theory (Helgeson and Kirkham, 1976). In the present study, the absolute solvation coefficient of the jth surface species is calculated using

$$\Omega^{abs.}_j = \frac{\eta Z_j^2}{4R_{e,j}} \quad (25)$$

where $R_{e,j}$ represents the effective electrostatic radius for the surface species, Z_j represents the charge on the jth species, and $\eta = 166.027$ kcal · Å · mole^{-1} (Sverjensky, 1993). By analogy with the effective electrostatic radii of aqueous species, which can be estimated based on crystallographic radii (Helgeson and Kirkham, 1976), it is proposed that the effective electrostatic radius of surface species can be expressed as

$$R_{e,j} = r_{x,j} + \gamma_Z \quad (26)$$

where $r_{x,j}$ represents a crystallographic radius and γ_z represents a constant for cations or anions of a given charge. Values of $r_{x,j}$ for cations and anions are given in Table 3. It will be shown below that the combination of Eqns. (23)–(26) can be used to explain variations in solvation behavior and to facilitate predictions for a wide range of cations.

2.2. Electrolyte Ion Adsorption

2.2.1. Thermodynamic Relations

Equilibria for adsorption of the monovalent electrolyte ions M^+ and L^- can be expressed by

$$>SOH + M^+ = >SO^-\_M^+ + H^+ \quad (27)$$

and

$$>SOH + H^+ + L^- = >SOH_2^+\_L^- \quad (28)$$

for which the equilibrium constants can be written as

$$*K^{\theta}_{M^+} = \frac{a_{>SO^-\_M^+} a_{H^+}}{a_{>SOH} a_{M^+}} 10^{\frac{F(\psi_\beta - \psi_0)}{2.303RT}} \quad (29)$$

and

$$*K^{\theta}_{L^-} = \frac{a_{>SOH_2^+\_L^-}}{a_{>SOH} a_{H^+} a_{L^-}} 10^{\frac{-F(\psi_\beta - \psi_0)}{2.303RT}} \quad (30)$$

where the superscript "*" represents the reaction written relative to $>SOH$ and the superscript "θ" represents the same standard states used above. For the reasons discussed above, activity coefficients for the surface species in Eqns. (29) and (30) can commonly be assumed to be unity. Possible exceptions in the case of amorphous silica under conditions far from the zero-point-of-change (ZPC) are discussed in the Appendix.

The standard states used in the present study can be expressed in terms of the hypothetical 1.0 Molar standard state by

$$*K^{\theta}_{M^+} = *K^{0}_{M^+} \left(\frac{N_s A_s}{N^{\ddagger} A^{\ddagger}} \right) \quad (31)$$

and

$$*K^{\theta}_{L^-} = *K^{0}_{L^-} \left(\frac{N_s A_s}{N^{\ddagger} A^{\ddagger}} \right) \quad (32)$$

Similarly, when the reactions are written relative to the charged surface species $>SOH_2^+$ and $>SO_+$,

$$>SO^- + M^+ = >SO^-\_M^+ \quad (33)$$

and

$$>SOH_2^+ + L^- = >SOH_2^+\_L^- \quad (34)$$

the equilibrium constants can be expressed

$$K^{\theta}_{M^+} = *K^{\theta}_{M^+} K^{\theta}_2 = *K^{0}_{M^+} K^{\theta}_2 \left(\frac{N_s A_s}{N^{\ddagger} A^{\ddagger}} \right) = \frac{a_{>SO^-\_M^+}}{a_{>SO^-} a_{M^+}} 10^{\frac{F\psi_\beta}{2.303RT}} \quad (35)$$

and

$$K^{\theta}_{L^-} = \frac{*K^{\theta}_{L^-}}{K^{\theta}_1} = \frac{*K^{0}_{L^-}}{K^{0}_1} \left(\frac{N_s A_s}{N^{\ddagger} A^{\ddagger}} \right) = \frac{a_{>SOH_2^+-L^-}}{a_{>SOH_2^+} a_{L^-}} 10^{\frac{-F\psi_\beta}{2.303RT}} \quad (36)$$

where the absence of the superscript "*" for adsorption of M^+ or L^- denotes the reaction written (as above) relative to $>SOH_2^+$ and $>SO^+$. It follows from the relations derived above that

$$K^{\theta}_{M^+} = K^{0}_{M^+} \quad (37)$$

and

$$K^{\theta}_{L^-} = K^{0}_{L^-} \quad (38)$$

In the present study, values of $*K^{0}_{M^+}$ and $*K^{0}_{L^-}$ obtained by regression of proton surface charge data are used to calculate values of $K^{\theta}_{M^+}$ and $K^{\theta}_{L^-}$ with the aid of Eqns. (35) and (36).

2.2.2. *Predictive Equations Based on Crystal Chemistry and Solvation Theory*

The standard Gibbs free energy of the νth electrolyte cation or anion adsorption reaction ($\Delta G^0_{r,\nu}$) is broken into three terms according to

$$\Delta G^0_{r,\nu} = \Delta G^0_{s,\nu} + \Delta G^0_{ai,\nu} + \Delta G^0_{ii,\nu} \quad (39)$$

where ($\Delta G^0_{s,\nu}$) represents a Born solvation contribution, ($\Delta G^0_{ai,\nu}$) represents an electrostatic interaction between the absorbate and near-surface species, and ($\Delta G^0_{ii,\nu}$) represents a term intrinsic to the aqueous adsorbate. The Born solvation term is treated by building on earlier studies of metal and electrolyte cation and anion adsorption (James and Healy, 1972; Sahai and Sverjensky, 1997b). The electrostatic interaction term for a cation is obtained by summing an attractive interaction between the cation and a surface oxygen with a repulsive interaction between the cation and the underlying metal of the solid sorbent. This treatment is analogous to that developed for adsorption of the H^+ cation (Yoon et al., 1979; Sverjensky and Sahai, 1996). The electrostatic interaction term for an anion is treated similarly to that for cations, i.e. an attractive interaction between the anion and the underlying metal of the solid and a repulsive interaction between the anion and the surface oxygen.

Assuming that the solvation contribution depends primarily on the inverse of the dielectric constant of the solid (ε_s) as described previously (Sverjensky and Sahai, 1996; Sahai and Sverjensky, 1997b) and that the electrostatic interaction terms depend primarily on the repulsive interactions described above results:

$$\log K^{\theta}_{M^+} = \frac{-\Delta\Omega_{r,M^+}}{2.303RT} \left(\frac{1}{\varepsilon_s} \right) - B_M \left(\frac{S}{r_{M^+}} \right) + \log K''_{ii,M^+} \quad (40)$$

and

$$\log K^{\theta}_{L^-} = \frac{-\Delta\Omega_{r,L^-}}{2.303RT} \left(\frac{1}{\varepsilon_s} \right) - B_L \left(\frac{2}{r_{L^-}} \right) + \log K''_{ii,L^-} \quad (41)$$

In Eqns. (40) and (41), the first term on the right-hand side represents the solvation term in Eqn. (39). The second term represents the repulsive interactions of the electrostatic term in Eqn. (39). The third term represents not only the intrinsic interactions in Eqn. (39), it also includes solvation contributions involving the interfacial dielectric constant and the electrostatic attractive interactions, all of which are approximated here to be constants for a given adsorbate.

The solvation terms in Eqns. (40) and (41) contain the symbols $\Delta\Omega_{r,M^+}$ and $\Delta\Omega_{r,L^-}$, which represent Born solvation coefficients for the reactions given by

$$\Delta\Omega_{r,M^+} = \Omega_{>SO^-\_M^+} - \Omega_{>SO^-} = \Omega^{abs.}_{>SO^-\_M^+} - \Omega^{abs.}_{>SO^-} \quad (42)$$

and

$$\Delta\Omega_{r,L^-} = \Omega_{>SOH_2^+\_L^-} - \Omega_{SOH_2^+} = \Omega^{abs.}_{>SOH_2^+\_L^-} - \Omega^{abs.}_{>SOH_2^+} \quad (43)$$

where the conventional and absolute Born coefficients are defined by Eqns. (23)–(26). The absolute Born coefficients ($\Omega^{abs.}_{>SO^-\_M^+}$ and $\Omega^{abs.}_{>SOH_2^+\_L^-}$) include a dependence on the inverse of the effective electrostatic radii of the cation and the anion

Table 4. Repulsion factor per angstrom $\left(\frac{2}{r_{L^-}}\right)$[a] for F^-, Cl^-, Br^-, I^-, HS^-, OH^-, NO_2^-, NO_3^-, CN^-, ClO_4^- for use in predictive equations involving Born solvation and crystal chemical theory.

Solid	$\frac{2}{r_{F^-}}$	$\frac{2}{r_{Cl^-}}$	$\frac{2}{r_{Br^-}}$	$\frac{2}{r_{I^-}}$	$\frac{2}{r_{HS^-}}$	$\frac{2}{r_{OH^-}}$	$\frac{2}{r_{NO_2^-}}$	$\frac{2}{r_{NO_3^-}}$	$\frac{2}{r_{CN^-}}$	$\frac{2}{r_{ClO_4^-}}$
Fe_3O_4	0.962	0.781	0.741	0.678	0.772	0.930	0.602	0.538	0.676	0.435
α-MnO_2	0.962	0.781	0.741	0.678	0.772	0.930	0.602	0.538	0.676	0.435
α-TiO_2	0.962	0.781	0.741	0.678	0.772	0.930	0.602	0.538	0.676	0.435
β-TiO_2	0.962	0.781	0.741	0.678	0.772	0.930	0.602	0.538	0.676	0.435
FeOOH	0.273	0.256	0.252	0.244	0.255	0.270	0.233	0.223	0.244	0.203
Fe_2O_3[b]	0.414	0.377	0.367	0.351	0.374	0.408	0.330	0.309	0.350	0.272
Fe_2O_3[c]	0.985	0.797	0.755	0.690	0.787	0.952	0.612	0.545	0.687	0.440
α-Al_2O_3	0.473	0.425	0.412	0.392	0.422	0.465	0.366	0.341	0.391	0.296
γ-Al_2O_3	0.473	0.425	0.412	0.392	0.422	0.465	0.366	0.341	0.391	0.296
$Al(OH)_3$	0.473	0.425	0.412	0.392	0.422	0.465	0.366	0.341	0.391	0.296
α-SiO_2	0.343	0.317	0.310	0.299	0.316	0.339	0.283	0.268	0.298	0.240
am. SiO_2[d]	0.375	0.344	0.336	0.323	0.343	0.370	0.304	0.287	0.322	0.255
am. SiO_2[e]	0.639	0.554	0.533	0.500	0.550	0.625	0.458	0.419	0.499	0.354

[a] Values of $\frac{2}{r_{L^-}}$ for the Lth anion calculated with values of r_{L^-} from Eqn. (45) and radii from Table 3.
[b] Hematites with pH_{ZPC} = 8.4–8.6.
[c] Hematites with pH_{ZPC} = 9.0–9.5 (intensively cleaned).
[d] DeGussa Aerosil amorphous silica.
[e] Other amorphous silicas, including Cabosil.

(Eqn. 25), which implies that values of $\Delta\Omega_{r,M^+}$ and $\Delta\Omega_{r,L^-}$ will depend inversely on ion size. Born solvation coefficients $\Delta\Omega_{r,M^+}$ and $\Delta\Omega_{r,L^-}$ are obtained in the present study by regression (see below) using known values of the dielectric constants of solids (Table 1).

The electrostatic terms in Eqns. (40) and (41) contain the crystal chemical parameters $\frac{s}{r_{M^+}}$ and $\frac{2}{r_{L^-}}$, where s represents the Pauling bond strength (Sverjensky and Sahai, 1996), and r_{M^+} and r_{L^-} represent the distances of the adsorbing ion being repulsed by the underlying cation of the solid and the surface oxygen, respectively. Values of these distances are estimated from the equations

$$r_{M^+} = r_{M-O} + \beta_{M^+,s} \tag{44}$$

and

$$r_{L^-} = r_{1,s} + r_{x,L^-} \tag{45}$$

where r_{M-O} represents the average metal oxygen bond length in a bulk crystal structure (Smyth and Bish, 1988) and $\beta_{M^+,s}$ represents values of the distance "β" in the triple-layer model predicted from a characteristic distance for each solid ($r_{1,s}$) and the size of the ion on the mineral surface, $r_{M^+,s}$ (Sverjensky, 2001) according to

$$\beta_{M^+,s} = r_{1,s} + r_{M^+,s} \tag{46}$$

Values of $r_{1,s}$ and $r_{M^+,s}$ are listed in Table 1 and discussed below. Consequently, the distance r_{M^+} is a predicted distance consistent with crystal structure analysis and a theoretical interpretation of capacitances (Sverjensky, 2001). In contrast, values of r_{L^-} cannot be calculated directly from values of β because triple-layer model capacitances do not depend on anion radii (Sverjensky, 2001). As a result, values of r_{L^-} are approximated using Eqn. (45), in which $r_{1,s}$ is added to an effective radius r_{x,L^-} (Shock and Helgeson, 1988). Values of $\frac{s}{r_{M^+}}$ and $\frac{2}{r_{L^-}}$ are given in Tables 2 and 4. They were used in the regression calculations described below to obtain the repulsion coefficients B_M and B_L and the "intrinsic" log K''_{ii,M^+}, and log K''_{ii,L^-}.

2.3. Capacitances

2.3.1. Theoretical Relations

The triple-layer model contains two capacitance parameters (C_1 and C_2). The value of C_1 directly impacts application of the model to proton surface charge data, which are the main focus of the present paper. The inner-layer capacitance (C_1) relates the charge at the innermost plane of adsorption (σ_0) to the drop in potential at a distance β according to

$$C_1 = \frac{\sigma_0}{\psi_0 - \psi_\beta} \tag{47}$$

where ψ_0 and ψ_β refer to the potentials at the 0-plane and the β-plane respectively. Because the surface potentials cannot be directly measured, the value of the capacitance C_1 is important in order to relate the potentials to the charge (σ_0).

Previous interpretations of triple-layer model capacitances relied on the properties of the electrolyte alone (Sahai and Sverjensky, 1997b) without accounting for the type of oxide or the state of hydration of the adsorbed ions. A more recent interpretation of model capacitances (Sverjensky, 2001) was facilitated by X-ray reflectivity studies of the rutile–electrolyte–water interface (Fenter et al., 2000). The latter provided fundamental constraints on distances of adsorbed species from mineral surfaces, which helps to ensure that the interpretation of model capacitances is consistent with physically reasonable values of the interfacial dielectric constant and the distance β.

Triple-layer model capacitances (C_1) for different mineral

surfaces fall into two groups (Sverjensky, 2001): on rutile, anatase, and magnetite, values of C_1 increase with decreasing crystallographic radius from Cs^+ to Li^+; on quartz, amorphous silica, goethite, hematite, and alumina, values of C_1 increase with decreasing hydrated cation radius from Li^+ to Cs^+. Consequently, on the first group, the alkalis are inferred to adsorb as dehydrated, inner-sphere complexes with sizes predictable from crystallographic radii. However, for the second group, the alkalis are inferred to adsorb as hydrated, outer-sphere complexes with sizes predictable from hydrated radii. This behavior can be described by a model of the interface which specifies a layer of chemisorbed water molecules at the surface and a layer of adsorbed alkali cations. The inverse capacitances of the two layers are summed in series yielding the approximation

$$\frac{1}{C_1} = \frac{r_{M^+,s}}{(8.854)\varepsilon_{\text{int.},s}} + \frac{r_{1,s}}{(8.854)\varepsilon_{\text{int.},s}} \tag{48}$$

where $r_{M^+,s}$ represents the radius of the adsorbed ion on the sth solid and $r_{1,s}$ represents part of the model distance $\beta_{M^+,s}$ (see Eqn. 46). Equation (48) is used below to regress model capacitances ($1/C_1$) with values of the electrolyte cation size ($r_{M^+,s}$, Table 1) yielding values for the coefficients $\varepsilon_{int.,s}$ and $r_{1,s}$. The resulting values of the interfacial dielectric constant and distance provide a firm physical interpretation of the model C_1 values.

The outer-layer capacitance C_2 refers to the drop in potential between the β- and d-planes of the triple-layer model. Consequently, for applications of the triple-layer model to calculations of proton surface charge only, the value of C_2 is unimportant. In the regressions of surface charge reported here, the value of $C_2 = 20\mu\text{F.cm}^{-2}$ was used. However, the value of C_2 is important for the prediction of ξ-potentials. An estimation method for the value of C_2 is developed below in order to ensure a physically reasonable interpretation of distances and dielectric constants.

3. CALIBRATION AND USE OF PREDICTIVE EQUATIONS FOR TRIPLE-LAYER MODEL PARAMETERS

3.1. Surface Protonation

3.1.1. Zero-Point-of-Charge Reaction

Values of the pH_{ZPC} reported in the literature characteristically show a range of values for any particular oxide (Kosmulski, 2002 and Table A1). Numerous reasons exist for these ranges (Kosmulski, 2002). These include differences in the definition of the pH_{ZPC} (Davis and Kent, 1990; Sposito, 1998), the experimental determination of the pH_{ZPC}, the way in which a sample was synthesized, and the way in which the surface was treated. The pH_{ZPC} is defined here to (ideally) reflect only the protonation reactions represented by Eqns. (1), (2), and (7). However, in experiments, proton surface charge development involves both proton/hydroxyl adsorption and coupled electrolyte ion adsorption at the surface. Consequently, the intersection point of surface titration curves corresponding to different ionic strengths, the point-of-zero-salt effect (pH_{PZSE}), can be expected to differ from the pH_{ZPC}. Values of the pH_{ZPSE} for a given solid can depend on the ionic strengths and on the electrolyte type used in the experiments (Lützenkirchen, 1998; Lützenkirchen and Magnico, 1998). In contrast, electrokinetic determinations of the isoelectric point (IEP) at low ionic strengths provide an absolute and more representative value of the pH_{ZPC}. In the present study, the selection of a single value of the pH_{ZPC} for each oxide has been made based on such isoelectric points. Where these were not available, the pH_{PZSE} for the lowest possible ionic strengths (e.g., 0.001–0.01 M) was used. Under these circumstances, it can be expected that the pH_{PZSE} provides a reasonable estimate of the pH_{ZPC}.

Literature values of the pH_{ZPC} for certain oxides also depend on the way in which the sample was synthesized and subsequently treated. For example, the pH_{ZPC} for rutile is taken here to be 5.4, based on surface titrations for a synthetic rutile which has been hydrothermally pretreated (Machesky et al., 1998). Without hydrothermal pretreatment, such rutiles release HCl left over from the synthesis. Similarly, the pH_{ZPC} of hematite has been taken to be 9.5, based on studies involving extensive washing of synthetic samples (Penners et al., 1986; Christl and Kretzschmar, 1999), without which the pH_{ZPC} is typically about 8.5, presumably because of impurities adsorbed to the surface. Finally, the pH_{ZPC} of goethite has been taken to be 9.2, based on studies involving extensive purging of the synthetic goethite to remove carbon dioxide. Without such purging of the surface, the pH_{ZPC} values of goethite can be much lower (Lumsden and Evans, 1994).

The values of pH_{ZPC} summarized in Table 5 were used to calculate values of log K_{ZPC} which were regressed with Eqn. (20) in terms of the parameters $\frac{1}{\varepsilon_s}$ and $\frac{s}{r_{H^+}}$ (Tables 1 and 2). Uncertainties in the experimental values of log K_{ZPC} are difficult to estimate because of the factors influencing pH_{ZPC} summarized above. However, it is likely that they are at least ± 0.3, which is less than the symbol size in Figure 1. It can be seen in Figure 1 that all the points agree closely with the regression line with the equation

$$\log K^{\theta}_{ZPC} = 36.7\left(\frac{1}{\varepsilon_s}\right) - 92.0\left(\frac{s}{r_{H^+}}\right) + 31.1 \tag{49}$$

The coefficients given in Eqn. (49) differ slightly from those given in previous studies (Sverjensky, 1994; Sverjensky and Sahai, 1996) for several reasons. First, based on the considerations discussed above, different zero points of charge for several minerals have been used in the present study (Table 5). Second, solids for which the dielectric constants are poorly known were omitted from the regression. These include goethite and hematite, whose dielectric constants have been estimated using the results of the regression calculations (Table 1).

3.1.2. del pK Reaction

The values of ΔpK^{θ}_n used previously (Sverjensky and Sahai, 1996) were again regressed in the present study with Eqn. (21) and values of $\frac{s}{r_{H^+}}$ from Table 2. Uncertainties in ΔpK^{θ}_n values are estimated here to be at least ± 0.3 based on the linear extrapolation technique employed by Davis et al. (1978). Slight differences from the previous results arise because the value of $\frac{s}{r_{H^+}}$ for γ-Al_2O_3 was reestimated using Eqn. (49) and the

Table 5. Experimental and calculated values of pH_{ZPC}, log K^{θ}_{ZPC}, ΔpK^{θ}_{n}, log K^{θ}_{1}, and log K^{θ}_{2} for the triple-layer model. Experimental values were taken from the sources noted. Calculated values were generated with Eqns. (49) and (50) and (11)–(13) together with values of ε_s, $\frac{s}{r_{H^+}}$ from Table 2.

Solid	pH_{ZPC} exptl.	pH_{ZPC} calc.	log K^{θ}_{ZPC} calc.	ΔpK^{θ}_{n} exptl.	ΔpK^{θ}_{n} calc.	log K^{θ}_{1} calc.	log K^{θ}_{2} calc.
Fe_3O_4	6.9[a]		14.8		5.7	4.6	10.3
α-MnO_2			9.9		6.4	1.8	8.2
α-TiO_2	5.4[b]	5.4	10.8	6.4[e]	6.3	2.3	8.6
β-TiO_2	6.0[c]		12.0		6.4	2.8	9.2
FeOOH	9.2[d]		18.4	6.6[e]	5.6	6.4	12.0
am. $Fe(OH)_3$	7.9[e]			5.6[e]	5.6	5.1	10.7
Fe_2O_3	9.5[f]	9.5	19.0		5.5	6.8	12.3
$Al_2Si_2O_{10}(OH)_4$	4.5[g]	4.4	8.8		7.0	0.9	7.9
α-Al_2O_3	9.4[h]	9.4	18.8		5.6	6.6	12.2
MgO	12.4[i]	12.5	25.0		4.8	10.1	14.9
γ-Al_2O_3	8.6[j]		17.1	5.8[e]	5.9	5.6	11.5
$Al(OH)_3$	10.0[k]	9.8	19.6		5.6	7.0	12.6
α-SiO_2	2.0[l]	2.0	4.0		8.4	−2.2	6.2
am. SiO_2	2.2[m]		5.6	8.4[e]	8.4	−1.4	7.0

[a] Blesa et al. (1984).
[b] Machesky et al. (1998).
[c] Sprycha (1984).
[d] Lumsden and Evans (1994).
[e] Davis et al. (1978).
[f] Christl and Kretzschmar (1999).
[g] Carroll-Webb and Walther (1985).
[h] Johnson et al. (1999).
[i] Parks (1965).
[j] Davis et al. (1978) analysis of data from Huang and Stumm (1973).
[k] Hiemstra et al. (1987).
[l] James and Healy (1972); Huang (1996).
[m] Average value of 2.0 (Franks, 2002) and 2.4 (Sonnefeld et al., 2001).

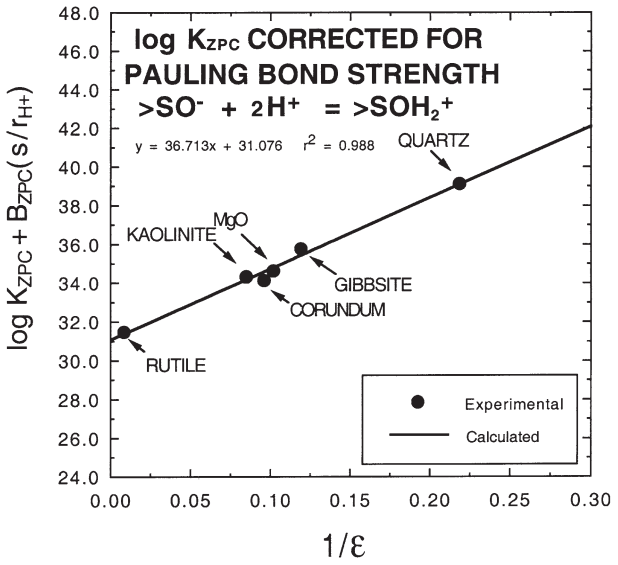

Fig. 1. Values of the logarithm of the equilibrium constant for the zero point of charge reaction (log K^{θ}_{ZPC}) as a function of the inverse of the dielectric constant $\left(\frac{1}{\varepsilon_s}\right)$ and values of the Pauling bond strength per Å $\left(\frac{s}{r_{H^+}}\right)$ from Tables 1 and 2. The symbols represent experimentally derived values whereas the solid line represents calculated values given in Table 5.

experimental value for the zero point of charge from Table 5. The resulting line of best fit shown in Figure 2 is consistent with the equation

$$\Delta pK^{\theta}_{n} = 13.1\left(\frac{s}{r_{H^+}}\right) + 3.4 \qquad (50)$$

Taken together Eqns. (49) and (50) enable predictions of the log K^{θ}_{ZPC} (and hence the zero points of charge) and the ΔpK^{θ}_{n} values of a wide range of solids. The predictions are summarized in Table 5 together with the values of log K^{θ}_{1} and log K^{θ}_{2} derived using Eqns. (11) and (12).

3.2. Electrolyte Ion Adsorption

Values of $^{*}K^{0}_{M^+}$, $^{*}K^{0}_{L^-}$, N_s, and A_s from Table A1, together with experimental values of pH_{ZPC} from Table A1 and predicted values of ΔpK^{θ}_{n} from Table 5, were used to calculate the logarithms of the electrolyte adsorption equilibrium constants log $K^{\theta}_{M^+}$ and log $K^{\theta}_{L^-}$ given in Table A1 with the equations

$$\log K^{\theta}_{M^+} = \log {}^{*}K^{0}_{M^+} + \log\left(\frac{N_s A_s}{N^{\ddagger} A^{\ddagger}}\right) + pH_{ZPC} + \frac{\Delta pK^{\theta}_{n}}{2} \qquad (51)$$

and

$$\log K^{\theta}_{L^-} = \log {}^{*}K^{0}_{L^-} + \log\left(\frac{N_s A_s}{N^{\ddagger} A^{\ddagger}}\right) - pH_{ZPC} + \frac{\Delta pK^{\theta}_{n}}{2} \qquad (52)$$

The values of $\log K^{\theta}_{M^+}$ and $\log K^{\theta}_{L^-}$ were used in the regression calculations described below (Figs. 3 and 4). A number of

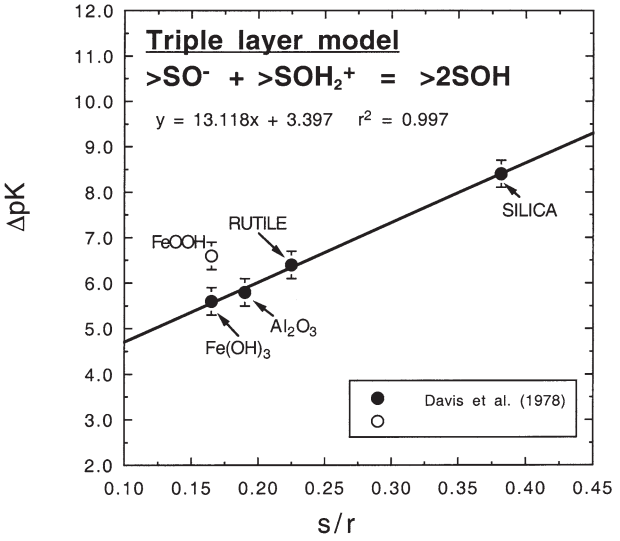

Fig. 2. Values of ΔpK_n^θ (i.e., $\log K_2^\theta - \log K_1^\theta$) as a function of the Pauling bond strength per Å $\left(\frac{s}{r_{H^+}}\right)$ from Table 2. The symbols represent experimentally derived values whereas the solid line represents calculated values given in Table 5.

values in Table A1 are not included in Figures 3 and 4 (rutile/$LiNO_3$, and goethite and hematite/KNO_3, Yates, 1975; rutile/KNO_3, Fokkink, 1987; quartz/NaCl, Riese, 1982; quartz/KNO_3, Huang, 1996; low BET hematite/$NaNO_3$, Gunnarsson et al., 2000; hematite/$NaClO_4$, Onoda and DeBruyn, 1966). It can be seen in Table A1 that these data are strongly discordant with the rest. Uncertainties in $\log K_{M^+}^\theta$ and $\log K_{L^-}^\theta$ are about ± 0.3 based on an estimation of the uncertainties in $\log^* K_{M^+}^0$ and $\log^* K_{L^-}^0$. These uncertainties are depicted as error bars on the points plotted in Figures 3 and 4. An additional source of uncertainty is discussed below.

3.2.1. Monovalent Cation Adsorption

Regression of the values of $\log K_{M^+}^\theta$ from Table A1 with Eqn. (40) in terms of the parameters $\frac{1}{\varepsilon_s}$ and $\frac{s}{r_{M^+}}$ from Tables 1 and 2 resulted in the lines of best fit shown in Figure 3 and the equations

$$\log K_{Li^+}^\theta + 10.0\left(\frac{s}{r_{Li^+}}\right) = -10.4\left(\frac{1}{\varepsilon_s}\right) + 5.2 \qquad (53)$$

$$\log K_{Na^+}^\theta + 8.0\left(\frac{s}{r_{Na^+}}\right) = -7.37\left(\frac{1}{\varepsilon_s}\right) + 4.4 \qquad (54)$$

$$\log K_{K^+}^\theta + 7.0\left(\frac{s}{r_{K^+}}\right) = -3.35\left(\frac{1}{\varepsilon_s}\right) + 3.70 \qquad (55)$$

$$\log K_{Cs^+}^\theta + 5.0\left(\frac{s}{r_{Cs^+}}\right) = -1.75\left(\frac{1}{\varepsilon_s}\right) + 3.5 \qquad (56)$$

$$\log K_{N(CH_3)_4^+}^\theta + 0.0\left(\frac{s}{r_{N(CH_3)_4^+}}\right) = 0.0\left(\frac{1}{\varepsilon_s}\right) + 3.4 \qquad (57)$$

It can be seen in Figure 3 that most of the datapoints agree closely with the regression lines within the uncertainties depicted. It should be noted, however, that there are larger discrepancies. For example, for Na^+ adsorption on goethite, the datapoints range from -0.3 to $+0.4$ with respect to the calculated value represented by the line. It is likely that the largest source of uncertainty contributing to such discrepancies is associated with the pH_{ZPC} values used to compute $\log K_{M^+}^\theta$ with Eqn. (51).

Values of the slopes $\left(\frac{\Delta\Omega_{r,M^+}}{-2.303RT}\right)$, intercepts ($\log K''_{ii,M^+}$), and repulsion parameters B_M from Eqns. (53)–(57) are summarized in Table 3 together with values of the Born solvation coefficient ($\Delta\Omega_{r,M^+}$) inferred from the slopes. It will be shown below that both ($\Delta\Omega_{r,M^+}$) and ($\log K''_{ii,M^+}$) can be predicted using a combination of Born solvation theory and empirical linear free energy correlations (Sahai and Sverjensky, 1997b).

Based on Born solvation theory and Eqns. (23)–(26) and (42), the values of ($\Delta\Omega_{r,M^+}$) inferred from the slopes in Figure 3 should correlate with the inverse of the effective electrostatic radius of the cation (R_{e,M^+}) according to

$$\Delta\Omega_{r,M^+} = \frac{\eta}{4R_{e,M^+}} - \Omega_{>SO^-}^{abs.} \qquad (58)$$

If it is assumed that the effective electrostatic radius can be calculated from the crystallographic radius (r_{x,M^+}, Eqn. 26 and Table 3) then the Born solvation coefficient can be expressed by

$$\Delta\Omega_{r,M^+} = \frac{\eta}{4(r_{x,M^+} + \gamma_+)} - \Omega_{>SO^-}^{abs.} \qquad (59)$$

where $\Omega_{>SO^-}^{abs.}$ and γ_+ are fit parameters. It can be seen in Figure 5 that Eqn. (59) is consistent with the values of $\Delta\Omega_{r,M^+}$ for Li^+, Na^+, K^+, and Cs^+ within the estimated uncertainties of about ± 1.5 cal · mole^{-1} with

$$\Omega_{>SO^-}^{abs.} = 14.5 \text{ kcal} \cdot \text{mole}^{-1} \qquad (60)$$

and

$$\gamma_+ = 0.70 \text{ Å} \qquad (61)$$

If the maximum value of $\Delta\Omega_{r,M^+}$ is 0.0 kcal · mole^{-1}, corresponding to a zero solvation effect, then the right-hand side of Eqn. (59) implies a limiting value of $r_{x,M^+} = 2.16$ Å. This implies that cations with radii larger than 2.16 Å should all have zero values of $\Delta\Omega_{r,M^+}$ and therefore zero slopes in plots such as those in Figure 3. Although the radius of $N(CH_3)_4^+$ is uncertain, it is much larger than this. Consequently, the dashed line corresponding to this cation in Figure 3 is drawn to be consistent with the limiting behavior of Eqn. (59).

Values of ($\log K''_{ii,M^+}$) for monovalent cations can be estimated from linear free energy correlations. In the present study, it is assumed that values of ($\log K''_{ii,M^+}$) represent the intrinsic binding of monovalent cations to a hypothetical oxide surface

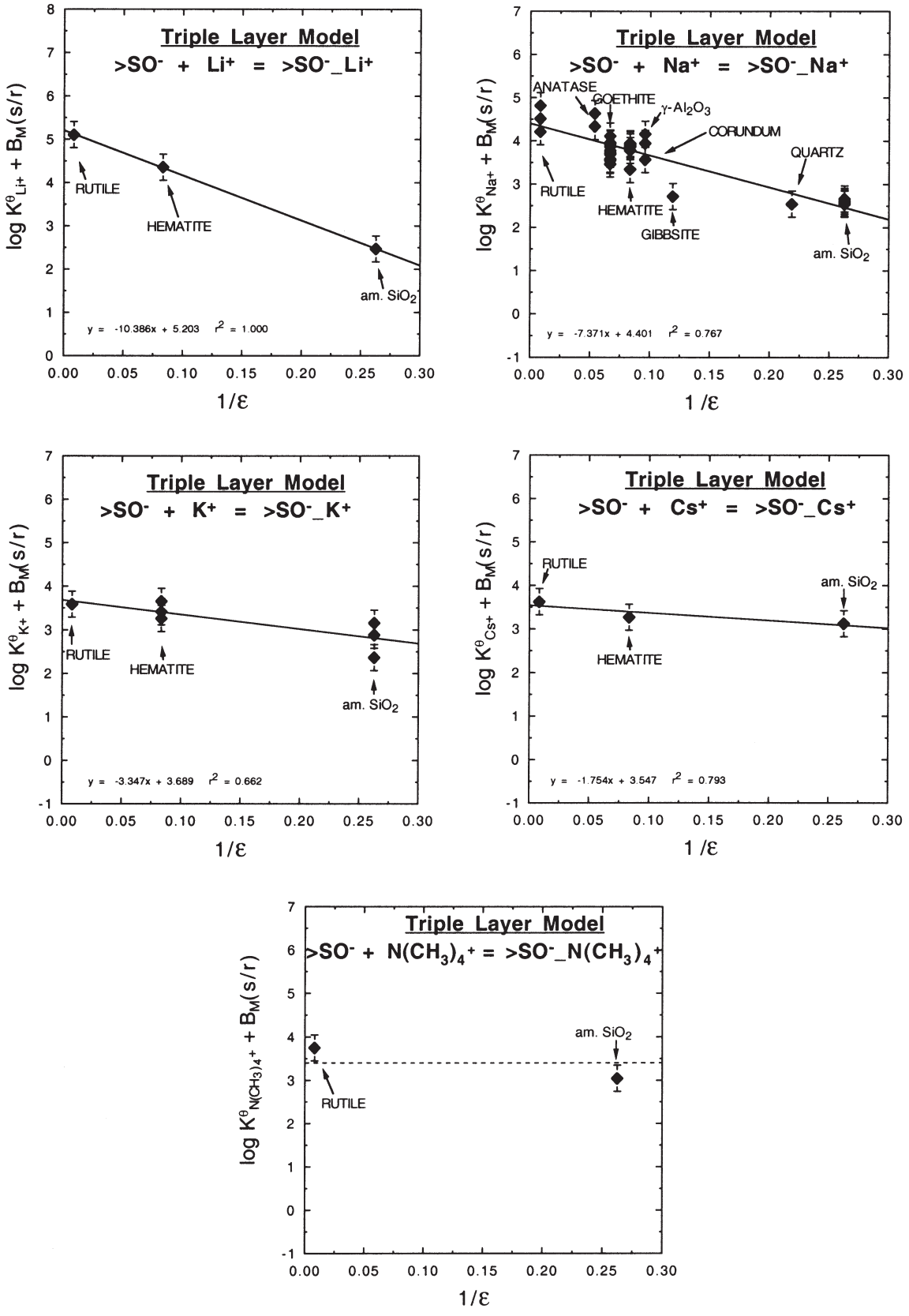

Fig. 3. Values of log K^{θ}_{M}, as a function of the inverse of the dielectric constant $\left(\frac{1}{\varepsilon_s}\right)$ and values of the Pauling bond strength per Å $\left(\frac{s}{r_{M^+}}\right)$ from Tables 1 and 2. The symbols represent experimentally derived values whereas the solid lines represent calculated values (see text).

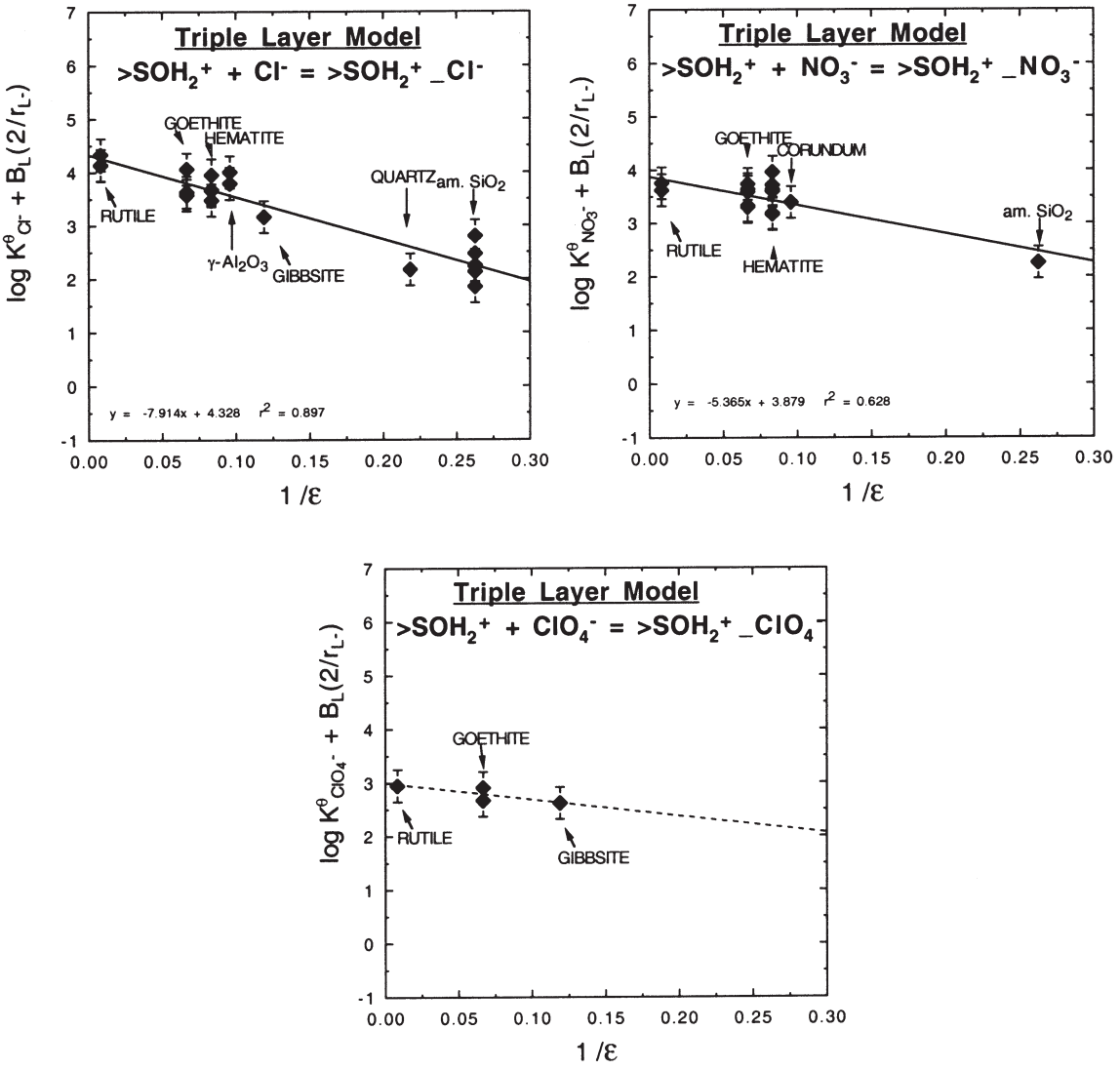

Fig. 4. Values of $K_{L^-}^{\theta}$ as a function of the inverse of the dielectric constant $\left(\frac{1}{\varepsilon_s}\right)$ and values of the bond strength per Å $\left(\frac{2}{r_{L^-}}\right)$ from Tables 1 and 4. The symbols represent experimentally derived values whereas the solid line represents calculated values (see text).

characterized by $\frac{1}{\varepsilon_s}$ and $\frac{s}{r_{M^+}}$ values of zero. In other words, values of ($\log K''_{ii,M^+}$) represent properties of the monovalent cation only. A number of possible cation properties could be used to construct a correlation with the values of ($\log K''_{ii,M^+}$). These include cation radius (Sahai and Sverjensky, 1997b) and solvation free energy of the aqueous cation (Sverjensky, 1993). In the present study, a linear free energy correlation with the equilibrium constant of the aqueous association reaction forming a metal–hydroxide complex was chosen.

It can be seen in Figure 6 that the values of ($\log K''_{ii,M^+}$) for Li^+, Na^+, and K^+ from the present study and Ag^+ from Davis and Leckie (1978) are consistent with the equation

$$\log K''_{ii,M^+} = 1.841(\log K_{M(OH)^0}) + 4.61 \qquad (62)$$

where $\log K_{M(OH)^0}$ refers to the equilibrium

$$M^+ + OH^- = M(OH)^0 \qquad (63)$$

Uncertainties in values of ($\log K''_{ii,M^+}$) are at least ±0.3 based on the correlations shown in Figure 3. Values of $\log K_{M(OH)^0}$ (Table 3) are not known for $Rb(OH)^0$ or $Cs(OH)^0$. But predicted values of ($\log K''_{ii,M^+}$) for Rb^+ and Cs^+ are given based on the limited regression data for adsorption of these species (see Table 3).

The equations and correlations summarized above permit the prediction of the equilibrium constant for the adsorption of monovalent electrolyte cations on any oxide. For example, the predicted values of $\log K_{M^+}^{\theta}$ in Table 6 have been calculated using the equation

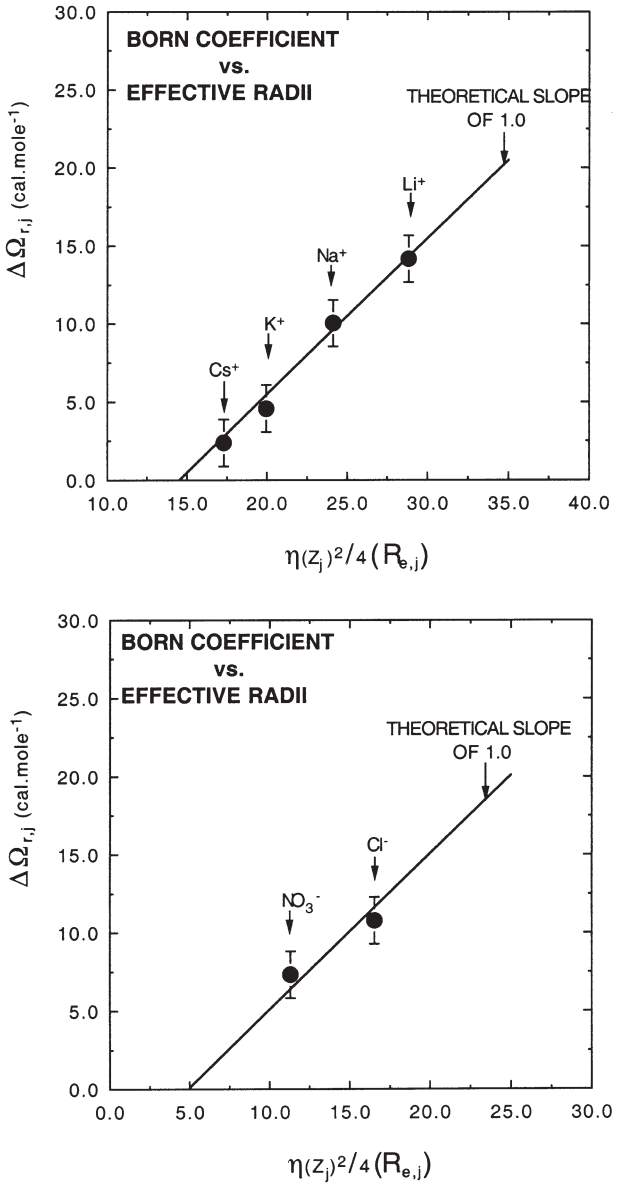

Fig. 5. Values of $\Delta\Omega_{r,j}$ as a function of the inverse of the effective electrostatic radius $\left(\frac{1}{R_{e,j}}\right)$ calculated with Eqn. (26) and values of $r_{x,j}$ (Table 3). The symbols represent values of $\Delta\Omega_{r,j}$ computed from the slopes of the lines in Figures 3 and 4 (Table 3), whereas the solid lines represent values calculated with Eqns. (59)–(61) and (71)–(73).

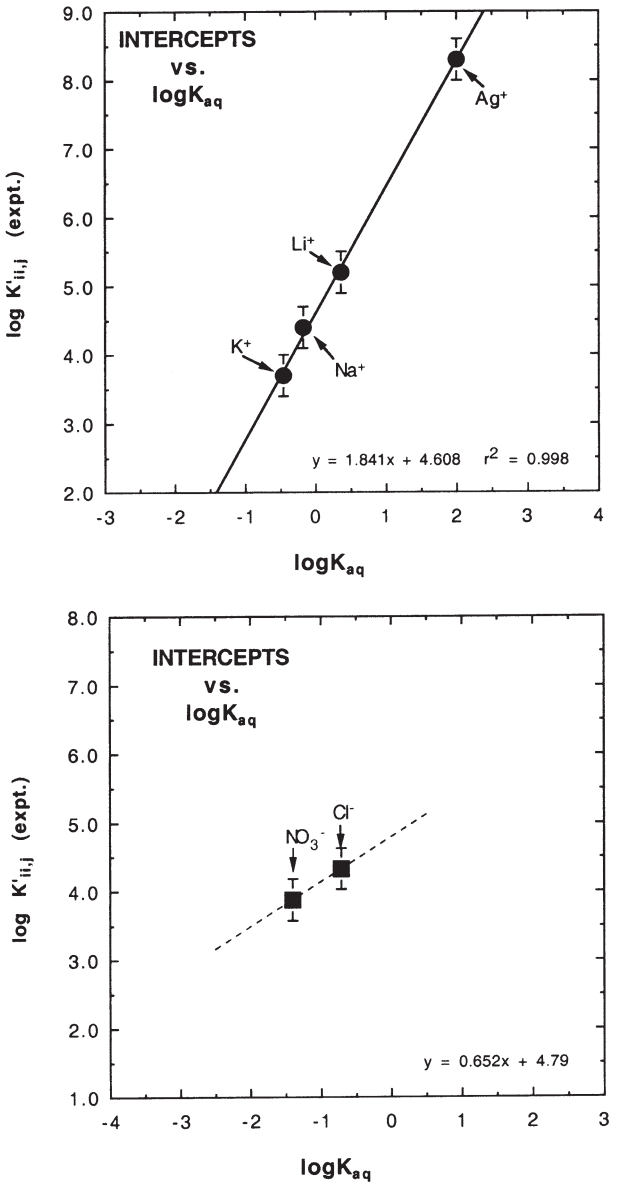

Fig. 6. Linear free energy correlations for values of $\log K''_{ii,M^+}$ and $\log K''_{ii,L^-}$ with the aqueous phase equilibrium association constants ($\log K_{M(OH)^0}$ and $\log K_{HL^0}$). The symbols represent the intercepts from Figures 3 and 4 (Table 3). The solid lines represent values calculated with Eqns. (62) and (75).

$$\log K^{\theta}_{M^+} = \frac{-\Delta\Omega_{r,M^+}}{2.303RT}\left(\frac{1}{\varepsilon_s}\right) - B_Z\left(\frac{s}{r_{M^+}}\right) + \log K''_{ii,M^+} \quad (64)$$

with values of $\Delta\Omega_{r,M^+}$ and ($\log K''_{ii,M^+}$) from Table 3 and values of ε_s and $\frac{s}{r_{M^+}}$ from Tables 1 and 2. Uncertainties in the predicted values of $\log K^{\theta}_{M^+}$ are at least ±0.3. It should perhaps be emphasized that the values of $\log K^{\theta}_{M^+}$ listed in Table 6 refer to standard states independent of the characteristics of the actual sample and to reactions involving adsorption onto the charged species $>SO^-$. However, in practice, most studies of surface charge still employ values of $\log {}^*K^{0}_{M^+}$ referring to the hypothetical 1.0 M standard state and reactions involving $>SOH$ written

$$>SOH + M^+ = >SO^-\_M^+ + H^+ \quad (65)$$

Predicted values of $\log {}^*K^{0}_{M^+}$ can be calculated from the values of $\log K^{\theta}_{M^+}$ summarized in Table 3 using

$$\log {}^*K^{0}_{M^+} = \log K^{\theta}_{M^+} - \log K^{\theta}_{2} - \log\left(\frac{N_s A_s}{N^{\ddagger} A^{\ddagger}}\right) \quad (66)$$

together with values of $\log K^{\theta}_2$ from Table 5 and values for N_s

Table 6. Predicted values of log $K^{\theta}_{M^+}$ where M^+ represents a monovalent cation at the β-plane of the triple-layer model[a].

		log $K^{\theta}_{M^+}$, for $>SO^- + M^+ = >SO^-\_M^+$								
Solid	ε_s[b]	Li^+	Na^+	K^+	Rb^+	Cs^+	Ag^+	Tl^+	NH_4^+	$N(CH_3)_4^+$
Fe_3O_4	1000	4.1	3.4	3.1	3.1	3.0	7.6	5.4	12.7	3.4
α-MnO_2	1000	3.3	2.8	2.6	2.7	2.7	7.1	5.0	12.3	3.4
α-TiO_2	121	3.3	2.8	2.6	2.7	2.7	7.1	5.0	12.3	3.4
β-TiO_2	18.6	2.8	2.5	2.4	2.5	2.6	6.9	4.8	12.1	3.4
FeOOH	15	4.1	3.4	3.2	3.2	3.1	7.6	5.5	12.8	3.4
Fe_2O_3[c]	12	3.8	3.2	3.0	3.0	3.0	7.4	5.3	12.6	3.4
Fe_2O_3[d]	12	3.0	2.6	2.6	2.7	2.8	7.0	5.0	12.3	3.4
α-Al_2O_3	10.4	3.6	3.0	2.9	2.9	2.9	7.3	5.2	12.5	3.4
γ-Al_2O_3	10.4	3.6	3.0	2.9	2.9	2.9	7.3	5.2	12.5	3.4
$Al(OH)_3$	8.4	3.4	2.9	2.8	2.8	2.9	7.1	5.2	12.4	3.4
α-SiO_2	4.6	1.8	1.7	2.0	2.1	2.4	6.3	4.4	11.7	3.4
am. SiO_2[e]	3.8	1.3	1.4	1.7	1.9	2.3	6.0	4.3	11.5	3.4
am. SiO_2[f]	3.8	0.8	0.9	1.3	1.5	2.0	5.5	3.8	11.1	3.4

[a] Calculated with Eqn. (61) and predicted values of $\Delta\Omega_{r,M^+}$ and log K''_{ii,M^+} from Table 3.
[b] Dielectric constant of the solid (see Table 2).
[c] Hematites with pH_{ZPC} = 8.4–8.6.
[d] Hematites with pH_{ZPC} = 9.0–9.5 (intensively cleaned).
[e] DeGussa Aerosil amorphous silicas.
[f] Other amorphous silicas including Cabosil.

and A_s characteristic of the solid. Alternatively, if an experimental value of the pH_{ZPC} is known, it should be used with predicted values of ΔpK^{θ}_n from Table 5 to calculate values of log*$K^0_{M^+}$ using

$$\log^* K^0_{M^+} = \log K^{\theta}_{M^+} - pH_{ZPC} - \frac{\Delta pK^{\theta}_n}{2} - \log\left(\frac{N_s A_s}{N^{\ddagger} A^{\ddagger}}\right) \quad (67)$$

Overall uncertainties in the calculated values of log*$K^0_{M^+}$ will reflect the uncertainties in the predicted values of log$K^{\theta}_{M^+}$ as well as the uncertainties in the pH_{ZPC} value of the sample of interest. It should be emphasized that the pH_{ZPC} input to Eqn. (67) should not be a point-of-zero-salt effect (pH_{PZSE}), because the equation already takes into account salt effects. Ideally, the pH_{ZPC} input to Eqn. (67) should be derived from a low ionic strength electrokinetic measurement (e.g., the IEP, see below for estimation of this quantity).

3.2.2. Monovalent Anion Adsorption

Regression of the values of log $K^{\theta}_{L^-}$ for Cl^- and NO_3^- derived from Table A1 with Eqn. (41) in terms of the parameters $\frac{1}{\varepsilon_s}$ and $\frac{s}{r_{L^-}}$ from Tables 1 and 4 resulted in the lines of best fit shown in Figure 4 and the equations

$$\log K^{\theta}_{Cl^-} + 2.0\left(\frac{2}{r_{Cl^-}}\right) = -7.91\left(\frac{1}{\varepsilon_s}\right) + 4.3 \quad (68)$$

$$\log K^{\theta}_{NO_3^-} + 2.0\left(\frac{2}{r_{NO_3^-}}\right) = -5.37\left(\frac{1}{\varepsilon_s}\right) + 3.9 \quad (69)$$

It can be seen in Figure 4 that most of the datapoints agree closely with the regression lines within the uncertainties depicted. As with the cation correlations in Figure 3, however, there are larger discrepancies. For example, for Cl^- adsorption on hematite, the datapoints range from −0.4 to +0.3 with respect to the calculated value represented by the line. Such discrepancies are also likely associated with the pH_{ZPC} values used to compute log $K^{\theta}_{L^-}$ with Eqn. (52).

Values of the slopes and intercepts and repulsion parameters (B_L) of Eqns. (68) and (69) are summarized in Table 3 together with values of $\Delta\Omega_{r,L^-}$ inferred from the slopes. It will be shown below that $\Delta\Omega_{r,L^-}$ and log K''_{ii,L^-} can also be predicted using a combination of Born solvation theory and empirical linear free energy correlations (Sahai and Sverjensky, 1997b).

Based on Born solvation theory and Eqns. (23)–(26) and (43), the values of $\Delta\Omega_{r,L^-}$ inferred from the slopes in Figure 4 should correlate with the value of the effective electrostatic radius of the anion (R_{e,L^-}) according to

$$\Delta\Omega_{r,L^-} = \frac{\eta}{4R_{e,L^-}} - \Omega^{abs.}_{>SOH_2^+} \quad (70)$$

Assuming that the effective electrostatic radius can be calculated from a crystallographic radius (r_{x,L^-}, Eqn. 26 and Table 3), the Born solvation coefficient can be expressed by

$$\Delta\Omega_{r,L^-} = \frac{\eta}{4(r_{x,L^-} + \gamma_-)} - \Omega^{abs.}_{>SOH_2^+} \quad (71)$$

where $\Omega^{abs.}_{>SOH_2^+}$ and γ_- are fit parameters.

It can be seen in Figure 5 that Eqn. (71) is consistent with the values of $\Delta\Omega_{r,L^-}$ for Cl^- and NO_3^- within the estimated uncertainties of about ±1.5 cal.mole^{-1} with

$$\Omega^{abs.}_{>SOH_2^+} = 4.9 \text{ kcal} \cdot \text{mole}^{-1} \quad (72)$$

and

$$\gamma_- = 0.70 \text{ Å} \quad (73)$$

Equations (71)–(73) permit prediction of the slopes for anions

Table 7. Predicted values of log $K^{\theta}_{L^-}$ where L^- represents a monovalent anion at the β-plane of the triple-layer model[a].

		log $K^{\theta}_{L^-}$ for $>SOH_2^+ + L^- = >SOH_2^+\_L^-$									
Solid	ε_s[b]	F^-	Cl^-	Br^-	I^-	HS^-	OH^-	NO_2^-	NO_3^-	CN^-	ClO_4^-
Fe_3O_4	1000	5.0	2.7	2.8	3.5	7.8	12.0	5.7	2.8	3.0	2.1
α-MnO_2	1000	5.0	2.7	2.8	3.5	7.8	12.0	5.7	2.8	3.0	2.1
α-TiO_2	121	4.9	2.7	2.8	3.5	7.8	11.9	5.6	2.8	2.9	2.1
β-TiO_2	18.6	4.3	2.3	2.4	3.2	7.4	11.5	5.4	2.6	2.6	2.0
FeOOH	15	5.6	3.2	3.3	4.0	8.3	12.6	6.1	3.1	3.1	2.4
Fe_2O_3[c]	12	5.1	2.8	2.9	3.6	8.0	12.2	5.8	2.9	2.8	2.2
Fe_2O_3[d]	12	4.0	2.0	2.1	2.9	7.1	11.1	5.2	2.4	2.4	1.9
α-Al_2O_3	10.4	4.8	2.6	2.7	3.5	7.7	11.9	5.6	2.8	2.7	2.1
γ-Al_2O_3	10.4	4.8	2.6	2.7	3.5	7.7	11.9	5.6	2.8	2.7	2.1
$Al(OH)_3$	8.4	4.6	2.4	2.5	3.3	7.6	11.7	5.5	2.7	2.5	2.0
α-SiO_2	4.6	3.7	1.8	2.0	2.8	6.9	10.9	5.1	2.3	2.0	1.8
am. SiO_2[e]	3.8	3.1	1.4	1.6	2.4	6.5	10.3	4.8	2.1	1.6	1.7
am. SiO_2[f]	3.8	2.5	1.0	1.2	2.1	6.1	9.8	4.5	1.8	1.4	1.5

[a] Calculated with Eqn. (74) and predicted values of $\Delta\Omega_{r,L^-}$, and log K''_{ii,L^-} from Table 3.
[b] Dielectric constant of the solid (see Table 2).
[c] Hematites with pH_{ZPC} = 8.4–8.6.
[d] Hematites with pH_{ZPC} = 9.0–9.5 (intensively cleaned).
[e] DeGussa Aerosil amorphous silicas.
[f] Other amorphous silicas including Cabosil.

for which data are sparse. Using r_{x,L^-} for ClO_4^- (Table 3) results in the slope shown in Figure 4 and an intercept consistent with

$$\log K^{\theta}_{ClO_4^-} + 2.0\left(\frac{2}{r_{ClO_4^-}}\right) = -3.1\left(\frac{1}{\varepsilon_s}\right) + 3.0 \qquad (74)$$

Values of log K''_{ii,L^-} for additional monovalent anions can be estimated from a linear free energy correlation similar to that derived above for cations. Assuming that values of log K''_{ii,L^-} are characteristic of the binding of monovalent anions to oxide surfaces, independent of the specific oxide, values of log K''_{ii,L^-} for Cl^- and NO_3^- are plotted in Figure 6. It can be seen in Figure 6 that the values of log K''_{ii,L^-} are consistent with the equation

$$\log K''_{ii,L^-} = 0.652(\log K_{HL^0}) + 4.79 \qquad (75)$$

where log K_{HL^0} refers to the equilibrium

$$H^+ + L^- = HL^0 \qquad (76)$$

Uncertainties in values of log K''_{ii,L^-} are at least ±0.3 based on the correlations shown in Figure 4.

The equations and correlations summarized above permit the prediction of the equilibrium constant for the adsorption of monovalent electrolyte anions on any oxide. For example, the predicted values of log$K^{\theta}_{L^-}$ in Table 7 have been calculated using the equation

$$\log K^{\theta}_{L^-} = \frac{-\Delta\Omega_{r,L^-}}{2.303RT}\left(\frac{1}{\varepsilon_s}\right) - B_L\left(\frac{2}{r_{L^-}}\right) + \log K''_{ii,L^-} \qquad (77)$$

with values of $\Delta\Omega_{r,L^-}$ and log K''_{ii,L^-} from Table 3 and values of ε_s and $\frac{2}{r_{L^-}}$ from Tables 1 and 4. Uncertainties in the predicted values of log$K^{\theta}_{L^-}$ are at least ±0.3. It should again be emphasized that the values of log$K^{\theta}_{L^-}$ listed in Table 7 refer to standard states independent of the characteristics of an actual sample and to reactions involving adsorption onto the charged species $>SOH_2^+$. Values of log*$K^{0}_{L^-}$ referring to the reaction

$$>SOH + H^+ + L^- = >SOH_2^+\_L^- \qquad (78)$$

can be calculated from the values of log $K^{\theta}_{L^-}$ summarized in Table 7 using

$$\log^* K^{0}_{L^-} = \log K^{\theta}_{L^-} + \log K^{\theta}_{1} - \log\left(\frac{N_s A_s}{N^{\ddagger} A^{\ddagger}}\right) \qquad (79)$$

together with values of log K^{θ}_1 from Table 5 and values for N_s and A_s characteristic of the solid of interest. Alternatively, if an experimental value of the pH_{ZPC} is known, it should be used with predicted values of ΔpK^{θ}_n from Table 5 to predict values of log*$K^{0}_{L^-}$ using

$$\log^* K^{0}_{L^-} = \log K^{\theta}_{L^-} + pH_{ZPC} - \frac{\Delta pK^{\theta}_n}{2} - \log\left(\frac{N_s A_s}{N^{\ddagger} A^{\ddagger}}\right) \qquad (80)$$

Overall uncertainties in the calculated values of log*$K^{0}_{L^-}$ will reflect the uncertainties in the predicted values of log$K^{\theta}_{L^-}$ as well as the uncertainties in the pH_{ZPC} value of the sample of interest. It should be emphasized that the pH_{ZPC} input to Eqn. (80) should not be a point-of-zero-salt effect (pH_{PZSE}), because the equation already takes into account salt effects. Ideally, the pH_{ZPC} input to Eqn. (80) should be derived from a low ionic strength electrokinetic measurement (e.g., the IEP; see below for estimation of this quantity).

3.3. Capacitances

Predictive equations based on Eqn. (48) for model capacitances (C_1) have been summarized previously (Sverjensky, 2001) for amorphous silica, quartz, hematite, goethite, γ-alu-

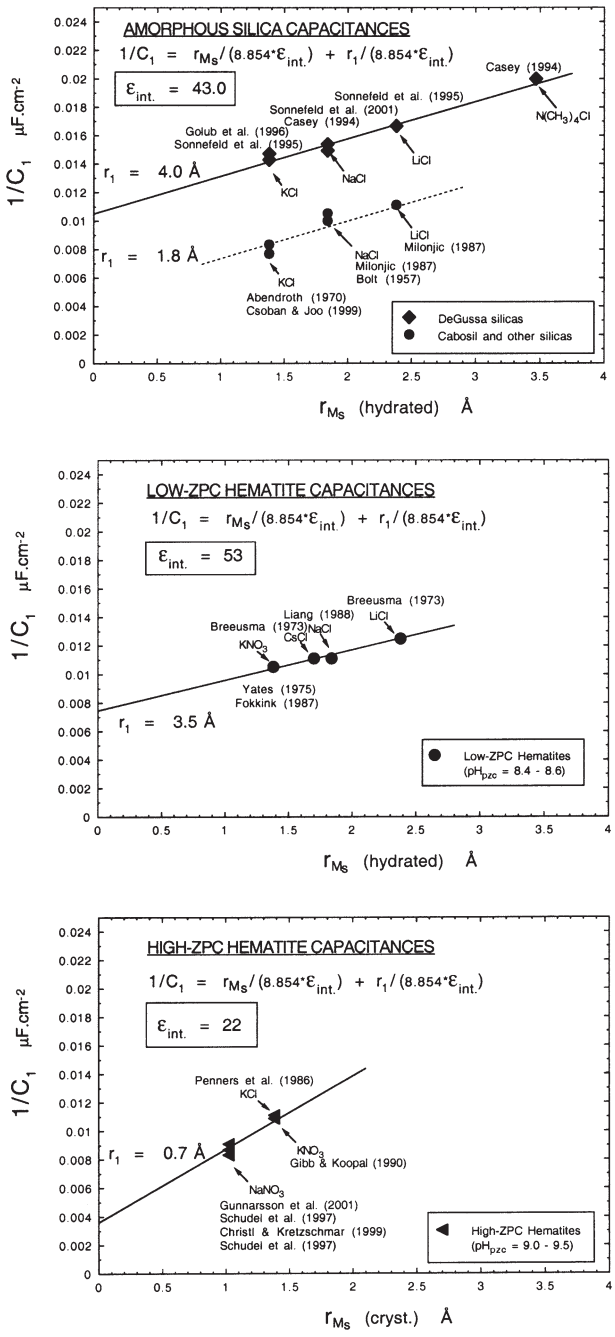

Fig. 7. Values of the inverse of the capacitance $\left(\frac{1}{C_1}\right)$ as a function of electrolyte cation size ($r_{M^+,s}$, Table 1). The symbols represent capacitances from Table A1. The lines represent values calculated with the equations and parameters shown (see text).

mina, corundum, rutile, anatase, and magnetite. The many additional, and in some cases revised, values of C_1 for amorphous silica, quartz, gibbsite, hematite, and goethite summarized in Table A1 enable new calibrations of Eqn. (48) for most of these minerals. Overall uncertainties in the capacitance values are probably of the order of $\pm 10\ \mu F \cdot cm^{-2}$. These are not depicted in Figure 7 for the sake of clarity.

3.3.1. Amorphous Silica and Quartz

It can be seen in Figure 7 that the values of $1/C_1$ for amorphous silicas define two separate correlations with electrolyte cation size ($r_{M^+,s}$). The upper line corresponds to DeGussa Aerosil silicas only, and is consistent with the equation

$$\frac{1}{C_1} = \frac{r_{M^+,s}}{(8.854)43} + \frac{4.0}{(8.854)43} \tag{81}$$

i.e., the interfacial dielectric constant $\varepsilon_{int.,s}$ and the distance $r_{1,s}$ are equal to 43 and 4.0 Å, respectively. The lower line corresponds to other types of amorphous silica, including Cabosil, and is consistent with the equation

$$\frac{1}{C_1} = \frac{r_{M^+,s}}{(8.854)43} + \frac{1.8}{(8.854)43} \tag{82}$$

The symbols in Figure 7 for cabosil and other silicas refer to capacitances generated by regression of surface charge data over a wide range of ionic strengths. Here the range of cation radii is more limited. Consequently, it has been assumed as a first approximation that the slope of the dashed line through these points is defined by the same interfacial dielectric constant ($\varepsilon_{int.,s} = 43$) as for the DeGussa silicas, resulting in a much smaller value of 1.8 Å for the distance of approach of the cations ($r_{1,s}$). The reason for the difference in capacitances between DeGussa and other silicas is not clear despite extensive reference to these silicas in the literature (Legrand, 1998; Papirer, 2000; Kosmulski, 2001). However, the model calculations shown in Figure 7 indicate that the different values of $r_{1,s}$ will result in repulsion parameters which are smaller for the DeGussa silicas than other amorphous silicas (Tables 2 and 4). This leads to predicted equilibrium constants for adsorption (Tables 6 and 7) that are stronger for the DeGussa silicas.

In the case of quartz, substantial uncertainty surrounds the prediction of the capacitance. Of the three data sets referred to in Table A1 (Riese, 1982; Michael and Williams, 1984; Huang, 1996), all of which refer to wide ranges of ionic strength, only the value of the log $K^{\theta}_{Na^+}$ from Michael and Williams (1984) is consistent with the results for other oxides, including the amorphous silicas. This suggests that there is only one reliable capacitance for quartz. Until additional studies of the proton surface charge of quartz are made over wide ranges of ionic strength, provisional estimates of the capacitances associated with adsorption onto quartz can be made based on the C_1 value derived from the data of Michael and Williams (1984). Assuming a value of $\varepsilon_{int.,s} = 43$ as for amorphous silica results in the equation

$$\frac{1}{C_1} = \frac{r_{M^+,s}}{(8.854)43} + \frac{4.5}{(8.854)43} \tag{83}$$

3.3.2. Gibbsite

The two values of C_1 equal to 40 and 60 $\mu F.cm^{-2}$ for gibbsite listed in Table A1 both refer to Na-electrolytes. However, only the sample with C_1 equal to 60 $\mu F.cm^{-2}$ has the high pH_{ZPC} expected for gibbsite. Assuming this value to be representative of gibbsite in Na-electrolytes, combined with $r_{1,s}$

= 2.9 (corresponding to alumina and corundum, Table 1) permits a provisional estimate of capacitances according to

$$\frac{1}{C_1} = \frac{r_{M^+,s}}{(8.854)} + \frac{2.9}{(8.854)32} \tag{84}$$

3.3.3. Hematite

It can be seen in Figure 7 that the values of $1/C_1$ for hematites also define two separate correlations with electrolyte cation size ($r_{M^+,s}$). The upper line corresponds to hematites with pH_{ZPC} values 8.4–8.6 and is consistent with the equation

$$\frac{1}{C_1} = \frac{r_{M^+,s}}{(8.854)53} + \frac{3.5}{(8.854)53} \tag{85}$$

i.e., the interfacial dielectric constant $\varepsilon_{int.,s}$ and the distance $r_{1,s}$ are equal to 53 and 3.5 Å, respectively, as previously published (Sverjensky, 2001). The lower line corresponds to hematites with pH_{ZPC} values 9.0–9.5 and is consistent with the equation

$$\frac{1}{C_1} = \frac{r_{M^+,s}}{(8.854)} + \frac{0.7}{(8.854)22} \tag{86}$$

It has been established that extensive cleaning of the surfaces of synthetic hematites raises the pH_{ZPC} as much as one unit (Penners et al., 1986). Presumably this is an indication of the desorption of cationic impurities remaining from the synthesis of the hematite. Adsorbed cationic impurities may repulse the adsorption of electrolyte cations, forcing them to bind at a greater distance from the impure surface compared to the clean surface. If so, this would decrease the capacitances for the low pH_{ZPC} hematites. This provides a physical basis for the differences in capacitance behavior between the two groups. The difference in the interfacial dielectric constants in Eqns. (85) and (86) also suggests that the structures of the water molecules near the two interfaces are different. Such effects have previously been suggested for titanium dioxides (Bourikas et al., 2001), but were not found for these solids in Sverjensky et al. (2001).

The difference in behavior of the two groups of hematites is even greater than that for the silicas, because the capacitances of the high-zpc hematites only yield a line with positive slope (Fig. 7) when dehydrated radii for the electrolyte cations are used. Although the data plotted in Figure 7 for this group refer to Na- and K-salts only, the C_1 values are behaving with radius like those for rutile. Other similarities with rutile can be seen in Table 1. The value of $\varepsilon_{int.,s}$ for the high-zpc hematites is small, comparable to that of rutile. Also, the very small values of $r_{1,s}$ = 0.7 and 0.75 Å imply that the adsorbing ions are close to the surface on both high-zpc hematites and rutile. A provisional conclusion that can be drawn is the notion that electrolytes are dehydrated when adsorbed on the surfaces of the high-zpc hematites and rutile.

3.3.4. Goethite

In contrast to the data analyzed for all other oxides, C_1 values for goethite are not consistent with radius correlations of the type discussed above. All 10 goethites listed in Table A1 refer to Na-electrolytes, but the C_1 values range from 60 to 145

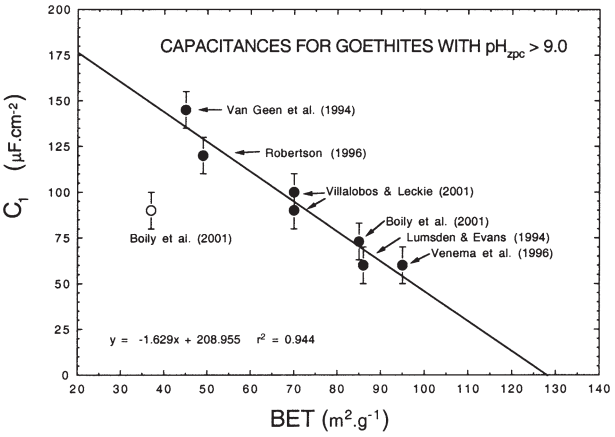

Fig. 8. Empirical correlation of the capacitance (C_1) of goethites with $pH_{ZPC} > 9.0$ as a function of BET surface area. The symbols represent capacitances from Table A1. The line represents calculated values (see text).

$\mu F \cdot cm^{-2}$. The reason for this is unclear. The effects of CO_2 lowering the pH_{ZPC} of goethite have been well-documented in the literature. But most of the goethites listed in Table A1 have $pH_{ZPC} > 9.0$ and have been purged of CO_2. Instead, it seems more likely that surface roughness effects associated with goethites with a range of BET values (Weidler et al., 1998) might be influencing the structure of the solid–water interface. Until studies of goethite surface charge for a given BET value in a variety of electrolytes are made, radius correlations do not seem useful for prediction of the capacitances of goethites.

In the present study, an empirical correlation between C_1 and the BET surface area for goethites with $pH_{ZPC} > 9.0$ is suggested for estimation purposes. For example, it can be seen in Figure 8 that, with the exception of one point, the values of C_1 for goethites correlate strongly with BET values ranging from about 50 to 100 $m^2 \cdot g^{-1}$. The line shown in Figure 8 is consistent with the equation

$$C_1 = (-1.63)BET + 209 \tag{87}$$

where C_1 is in $\mu F \cdot cm^{-2}$ and BET is in $m^2 \cdot g^{-1}$.

3.3.5. Summary of Predicted Capacitances

Predicted values of C_1 for DeGussa amorphous silica, other amorphous silicas, quartz, high-zpc hematite and gibbsite based on Eqns. (81)–(86), together with values previously predicted for rutile, anatase, magnetite, and low-zpc hematite, γ-alumina, and corundum (Sverjensky, 2001) are summarized in Table 8 for a range of monovalent electrolyte cations.

4. PREDICTION OF PROTON SURFACE CHARGE

4.1. Comparison of Prediction and Experiment

The equations summarized above permit prediction of the equilibrium constants for surface protonation (pH_{ZPC} and ΔpK_n^θ), electrolyte adsorption (log $K_{M^+}^\theta$ and log $K_{L^-}^\theta$), and the values of the inner-layer capacitance (C_1). Predicted values of these parameters (summarized in Tables 5, 6, 7, and 8), together with site densities, BET surface areas, and the outer-

Table 8. Predicted values of the capacitance C_1 ($\mu F \cdot cm^{-2}$) for the triple-layer model[a].

Solid	Li^+	Na^+	K^+	Rb^+	Cs^+	NH_4^+	$N(CH_3)_4^+$
Fe_3O_4	155	131	108	103	94	104	55
α-MnO_2	155	131	108	103	94	104	55
α-TiO_2	155	131	108	103	94	104	55
β-TiO_2	155	131	108	103	94	104	55
Fe_2O_3[b]	80	88	96	94	90	94	67
Fe_2O_3[c]	135	113	94	90	81	90	47
α-Al_2O_3	89	99	107	107	103	107	74
γ-Al_2O_3	89	99	107	107	103	107	74
$Al(OH)_3$	54	60	66	65	62	65	45
α-SiO_2	55	60	65	64	61	64	48
am. SiO_2[d]	60	65	71	70	67	70	51
am. SiO_2[e]	91	105	120	116	109	116	72

[a] Values for Fe_3O_4, α-MnO_2, α-TiO_2, β-TiO_2, Fe_2O_3[b], α-Al_2O_3, and γ-Al_2O_3 from Sverjensky (2001). Values for other solids calculated with Eqns. (81)–(86) using interfacial dielectric constants and distance parameters from Table 1.
[b] Hematites with $pH_{ZPC} = 8.4–8.6$.
[c] Hematites with $pH_{ZPC} = 9.0–9.5$ (intensively cleaned).
[d] DeGussa Aerosil amorphous silicas.
[e] Other amorphous silicas including Cabosil.

layer capacitance (C_2), permit triple-layer model predictions of proton surface charge for an oxide in a 1:1 electrolyte solution in the absence of any other experimental data. A major uncertainty in such predictions arises from the likelihood that the pH_{ZPC} of an actual sample may differ from the predicted value because of differences in sample synthesis or surface treatment. More accurate predictions of proton surface charge are likely if they are based on an experimental value of the pH_{ZPC} from electrokinetic measurements at low ionic strengths. Examples of such predictions are shown in Figure 9 for rutile in LiCl and CsCl, and hematite in $NaNO_3$. It can be seen in Figure 9 that the calculated curves for proton surface charge agree with the data in most instances within about 10%. Larger discrepancies typically occur at pH values farthest away from the pH_{PZSE}, where uncertainties in predicted values of log $K^{\theta}_{M^+}$, log $K^{\theta}_{L^-}$, or C_1 are magnified. Although not often reported, experimental uncertainties at these pH values are also probably maximal.

It should be noted that the predicted proton surface charge curves do not depend significantly on the values of ΔpK^{θ}_n or C_2. However, predicted values of the zeta potential (calculated assuming $\zeta = \psi_d$) do depend strongly on these parameters, as well as on log $K^{\theta}_{M^+}$, log $K^{\theta}_{L^-}$, or C_1. In the present study, values of ΔpK^{θ}_n are predicted using the crystal-chemical correlation in Figure 2. Values of C_2 are subject to more uncertainty. Traditionally, in applications of the triple-layer model a value of $C_2 = 20 \mu F \cdot cm^{-2}$ has been used (Yates, 1975; Davis et al., 1978). However, this small value implies rather large distances between the β- and the d-planes in the model. Recent molecular dynamics studies have suggested that the total distance from the (110) surface of rutile to water molecules with bulk properties is about 10–15 Å (Zhang et al., 2004). This distance, together with the dielectric constant for bulk water at 25°C, suggests that larger values of C_2 would be more appropriate. In the present study, it has been assumed that the separation of the β- and the d-planes is influenced by the size of the electrolyte cation on the β-plane by taking $C_1 = C_2$. It can be seen in Figure 9 that the agreement between the curves representing predicted zeta potentials and the experimental data supports the values of ΔpK^{θ}_n and C_2 predicted in the present study. The agreement is clearly best within about 2 pH units of the IEP and at ionic strengths of about 0.01 M.

The predicted values of C_2 shown in Figure 9 imply model distances between the β-plane and the d-plane of 4.5, 7.3, and 6.1 Å for rutile in LiCl and CsCl, and hematite in $NaNO_3$, respectively (assuming the dielectric constant of water between the planes is 78). Based on the values of C_1 shown in Figure 9, the corresponding model distances between the o-plane and the β-plane are 1.5, 2.5, and 1.7 Å (assuming the dielectric constant of water between the planes is 26 for rutile and 22 for hematite, Table 1). Consequently, model values for the total distance between the 0- and the d-planes are 6.0, 9.8, and 7.8 Å, respectively. For rutile, the model 0-plane may be about 1.2 Å above the (110) surface (Sverjensky, 2001). Adding this approximate distance to the values derived for rutile in LiCl and CsCl results in distances of about 7.2 and 11.0 Å, respectively, which overlaps with the estimates from molecular dynamics.

In summary, the equations and data given above permit prediction of the proton surface charge in reasonable agreement with experimental data. The triple-layer model parameters predicted here also imply interfacial dielectric constants and distances of the bound electrolyte ions from the surface that are consistent with the results of X-ray studies (Sverjensky, 2001). In addition, the zeta potentials implied by the predictive triple-layer model are in reasonable agreement with the results of electrokinetic experiments, and the implied total distances from the surface to the shear plane are consistent with molecular dynamics results. These overall agreements provide support for the use of the triple-layer model in a predictive mode. Examples of this are discussed below.

4.2. Trends in Electrolyte Binding to Oxide Surfaces

The predicted strengths of electrolyte equilibrium adsorption constants can be expected to vary systematically with different types of electrolyte ions and solids because of the explicit dependence on ionic radius and characteristics of the solid associated with Born solvation and crystal chemical theory (Eqns. 40 and 41) and also because of the free energy correla-

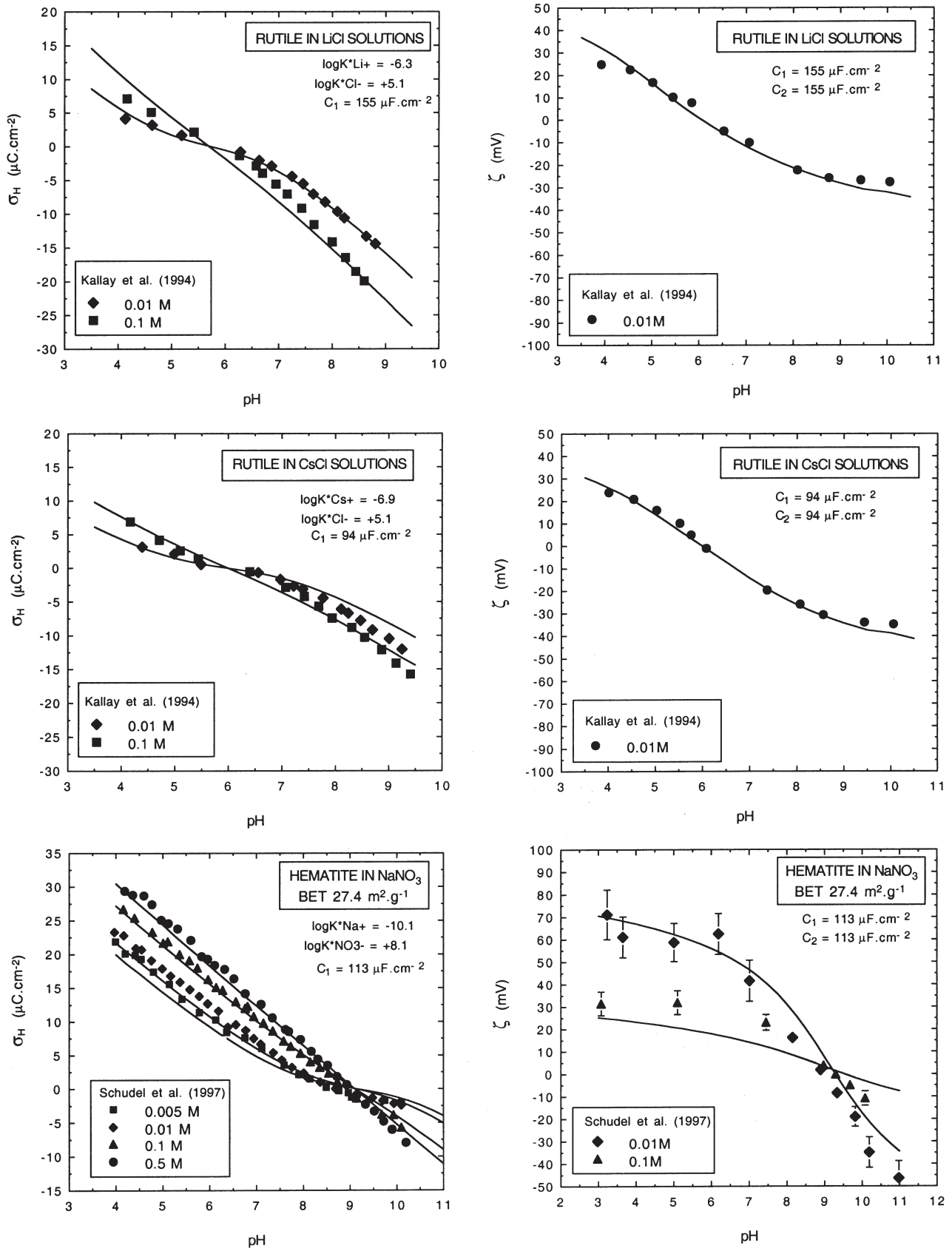

Fig. 9. The solid curves represent predicted values of the proton surface charge and zeta potential on rutile and hematite as a function of pH calculated with equilibrium constants from Tables 6 and 7 and capacitances from Table 8. The experimental data were taken from the sources given in the figure.

tions adopted for the ion-intrinsic equilibrium constants (Eqns. 62 and 75). For example, trends for the alkali cations with ion size and dielectric constant can be seen in Table 6. For any given cation, the predicted equilibrium constants tend to decrease with decreasing dielectric constant of the solid. However, the behavior of high dielectric constant solids differs from that of low dielectric constant solids. For example, on Fe_3O_4, α-MnO_2, α-TiO_2, and β-TiO_2, equilibrium constants decrease with increasing alkali cation size from Li^+ through Cs^+. In contrast, on α-SiO_2 and amorphous SiO_2, equilibrium constants increase with increasing alkali cation size from Li^+ through Cs^+. Such trends can be explained by rewriting Eqn. (40) as

$$\log K^{\theta}_{M^+} + B_M\left(\frac{s}{r_{M^+}}\right) = \frac{-\Delta\Omega_{r,M^+}}{2.303RT}\left(\frac{1}{\varepsilon_s}\right) + \log K''_{ii,M^+} \quad (88)$$

For solids with the smallest values of $\frac{1}{\varepsilon_s}$ (e.g., rutile), it can be seen in Table 6 that the predicted equilibrium constants increase in the sequence Cs^+ and Rb^+, K^+, Na^+, Li^+. In contrast, for solids with the largest values of $\frac{1}{\varepsilon_s}$ (e.g., amorphous silica), the predicted sequence is Li^+, Na^+, K^+, Rb^+, Cs^+. Solids with intermediate values of $\frac{1}{\varepsilon_s}$ (e.g., hematite and gibbsite, and other iron and aluminum oxides and hydroxides) will have predicted equilibrium adsorption constants that are roughly independent of the type of adsorbing alkali cation. The reasons for this behavior lie in Eqn. (88).

The first term on the right-hand side of Eqn. (88) results from Born solvation theory. This term is negligable for solids such as rutile with high dielectric constants. Consequently, the equilibrium constants for these solids vary because of the ion-intrinsic term $\log K''_{ii,M^+}$, which depends on a linear free energy correlation (Eqn. 62). This leads to an increase in equilibrium constants in the sequence Cs^+, Rb^+, K^+, Na^+, Li^+. Such increases will contribute to increasing the predicted proton surface charge in the same sequence.

When Eqn. (88) describes low dielectric constant solids such as quartz or amorphous silica, the first term on the right-hand side of the equation becomes substantial. From Born solvation theory, values of $\Delta\Omega_{r,M^+}$ vary inversely with crystallographic radius (Eqn. 59). Consequently, the first term on the right-hand side of Eqn. (88) becomes more negative in the sequence Cs^+, Rb^+, K^+, Na^+, Li^+. This trend opposes the trend of the second term with free energy. As a result, adsorption on solids such as amorphous silica results in predicted equilibrium constants increasing in the sequence Li^+, Na^+, K^+, Rb^+, Cs^+ (the reverse of that predicted for rutile and high dielectric constant solids). The predicted sequence for solids such as silica will contribute to increasing the predicted proton surface charge with the same sequence of alkalis.

For solids with dielectric constants intermediate to those of rutile and silica, e.g., iron and aluminum oxides and hydroxides, the systematically changing terms discussed above result in the alkalis adsorbing on these solids to a similar extent. Experimentally measured zeta potentials for corundum in dilute alkali nitrate solutions (Johnson et al., 1999) are in qualitative agreement with the predictions of Table 6. At ionic strengths of 0.01 M, the zeta potentials at any given pH value above the point-of-zero charge show very small changes, becoming more positive in the sequence Cs^+ or K^+, Na^+, Li^+. Changes for 1.0 M solutions are more substantial. It is also interesting to note that the predicted similarities for alkali cation adsorption on iron and aluminum oxides and hydroxides might help to explain the applicability of surface complexation models such as the diffuse double layer model (Dzombak and Morel, 1990) and the constant capacitance model (Schindler and Stumm, 1987; Lövgren et al., 1990) which do not explicitly take into account the binding of electrolyte ions. If the alkali ions adsorb to about the same extent on these oxides, then the neglect of electrolyte ion binding is a reasonable approximation for a given ionic strength.

In summary, the simple solvation theory used in Eqn. (88) indicates that when alkalis adsorb onto high dielectric constant solids there is no significant opposing free energy of solvation (James and Healy, 1972). It is thus comparatively easy for the waters of solvation on ions to be removed as they adsorb to the rutile surface. If so, it can be expected that the alkalis can form inner-sphere complexes at the rutile–water interface (Sverjensky, 2001), as seems to be required by X-ray standing-wave studies (Fenter et al., 2000). In contrast, when alkalis adsorb onto low dielectric constant solids there is a very significant opposing free energy of solvation. If it is difficult for the waters of solvation on cations to be removed as they adsorb to the silica surface, it can be expected that the alkalis form outer-sphere complexes at the silica–water interface (Sverjensky, 2001). This inference has yet to be tested by X-ray standing-wave studies.

4.3. Trends in Proton Surface Charge With Electrolyte Type

The trends discussed above suggest that rutile and amorphous silica are end-members showing opposite behavior with respect to cation binding. In order to demonstrate the consequences of this behavior for proton surface charge, specific predictions are depicted for rutile and amorphous silica in Figure 10 referring to 0.1 M ionic strength. It should be noted that prediction of proton surface charge with the triple-layer model depends not only on the predicted electrolyte equilibrium constants but also on predicted model capacitances. On high dielectric constant solids such as rutile, model capacitances are predicted to increase in the same sequence as the equilibrium constants (Sverjensky, 2001, Table 8). Both factors contribute to increasingly negative proton surface charge at a given $pH > pH_{ZPC}$. As a result, the predicted proton surface charge on rutile and similar solids (at a given $pH > pH_{ZPC}$ and ionic strength) becomes increasingly negative in the sequence Cs^+, Rb^+ and K^+, Na^+, Li^+(Fig. 10). This result is consistent with experimental observations (Bérubé and Bruyn, 1968; Sprycha, 1984; Kallay et al., 1994). It is the reverse of the classical lyotropic sequence for the adsorption of the alkalis on Hg and AgI, as already noted by Kallay et al. (1994).

A trend for anion adsorption on rutile is also shown in Figure 10. Here predicted surface charges for rutile in 0.1 M solutions of $NaCl$, $NaNo_3$ and $NaClO_4$ solutions are compared. It can be seen that surface charge at a given pH increases from ClO_4^- to NO_3^- and Cl^-. This is a direct consequence of the sequence of

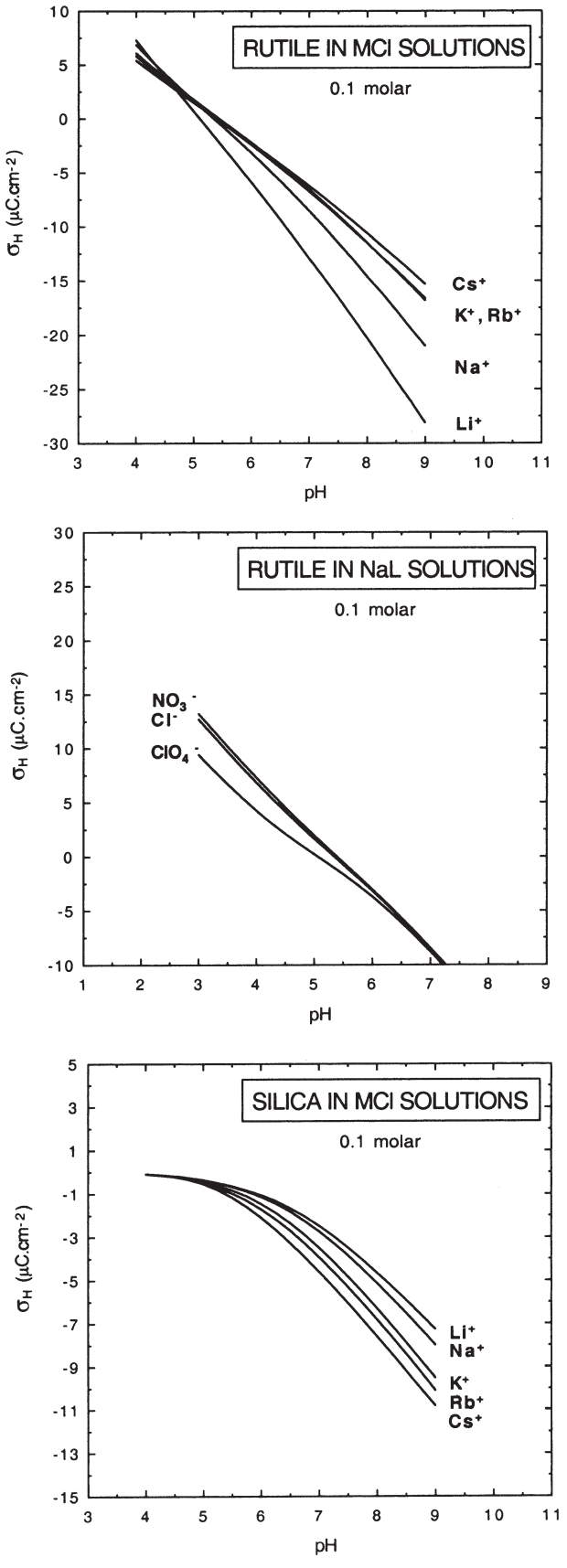

anion binding predicted in Table 7. As noted above, solvation effects are negligable on rutile, consequently the predicted sequence of anion binding comes directly from the intrinsic binding in Eqn. (75), which depends only on a free energy correlation. The sequence shown in Figure 10 is consistent with experimental results (Bérubé and De Bruyn, 1968b; Kallay et al., 1994) and previous models of the rutile–water interface (Bourikas et al., 2001).

On amorphous silica, model capacitances are predicted to increase in the sequence Li^+, Na^+, K^+, and then to decrease from Rb^+ to Cs^+ (Table 8). However, the differences are rather small. A stronger trend is exhibited by the equilibrium constants for cation binding in Table 6. As a consequence, the predicted proton surface charge on silica (at given $pH > pH_{ZPC}$ and ionic strength) becomes increasingly negative in the sequence Li^+, Na^+, K^+, Rb^+, Cs^+. These predicted results for silica are also consistent with experimental observations (Dugger et al., 1964; Tadros and Lyklema, 1968; Abendroth, 1970; Sonnefeld et al., 1995; Karlsson et al., 2001; Zuyi and Hongxia, 2002).

4.4. Prediction of Point-of-zero-salt Effects (pH_{PZSE} vs. pH_{ZPC})

Although considerable attention has been paid to the issue of how best to use the point-of zero-salt effect (pH_{PZSE}) relative to the pH_{ZPC} (Davis and Kent, 1990; Lützenkirchen and Magnico, 1998; Sposito, 1998), few attempts have been made to predict the magnitude of salt effects (Rudzinski et al., 2000; Sonnefeld, 2001). The pH_{PZSE} for a given solid in different electrolytes can differ from the pH_{ZPC} defined by low ionic strength electrokinetic data because of the assymetrical binding strengths of cations and anions.

From a practical standpoint, assymetrical binding strengths of a cation and anion in a salt solution can be manifested in several ways. First, assymetry is manifested in titration data when the intersection points of three or more titration curves are not coincident and change systematically with ionic strength. Second, more frequently, the intersection points of three or more titration curves are coincident (pH_{PZSE}) within the uncertainties of judging the slopes of the curves. However, when electrokinetic measurements are made on the same samples, the IEP defined by the lowest ionic strength is different to the pH_{PZSE} (Huang and Stumm, 1973; Yates, 1975; Fokkink, 1987; Zeltner and Anderson, 1988; Gibb and Koopal, 1990; Kallay et al., 1994; Trivedi and Axe, 2001; Rosenqvist et al., 2002). Finally, assymetrical binding is also indicated when surface titrations of a single sample in different electrolytes reveal different pH_{PZSE} values (Maneepong and Wada, 1991; Villalobos and Leckie, 2001). It will be shown below that a very simple prediction of the relative strengths of cation and anion binding can be used to indicate the assymetry of ion

Fig. 10. Predicted trends of the proton surface charge as a function of electrolyte type for rutile and DeGussa silica in 0.1 M solutions. The curves were calculated with predicted equilibrium constants from Tables 6 and 7 and capacitances from Table 8.

binding to be expected and the difference between the IEP and the pH_{PZSE}.

The difference between the IEP and the pH_{PZSE} can be obtained by combining the equilibria in Eqns. (33) and (34) to give

$$>SOH_2^+ + L^- + >SO^-\_M^+ = >SOH_2^+\_L^- + M^+ + >SO^- \quad (89)$$

Assuming that the activities of M^+ and L^- are equal permits the mass action expression corresponding to Eqn. (89) to be rearranged, yielding

$$pH_{PZSE} - IEP = 0.5(\log K^{\theta}_{L^-} - \log K^{\theta}_{M^+}) \quad (90)$$

Point-of-zero-salt effects for surface titration curves can thus be predicted using the difference $\log K^{\theta}_{L^-} - \log K^{\theta}_{M^+}$ obtainable from Tables 6 and 7. It can be seen from Eqn. (90) that when the anion binds more strongly than the cation, the pH_{PZSE} will lie above the *IEP*. However, when the cation binds more strongly than the anion, the pH_{PZSE} will lie below the *IEP*. It should be stressed that the *IEP* (corresponding to low ionic strengths) is being used here as an approximation to the pristine point-of-zero charge. It can be seen in Tables 6 and 7 that cations and anions are predicted to bind with different strengths depending on the solid and the electrolyte. Consequently, the pH_{PZSE} should in general differ from the pristine point-of-zero charge because of differences in cation and anion binding.

The applicability of Eqn. (90) can be assessed with the aid of the experimental data shown in Figure 11. In the uppermost graph, experimental measurements of the difference between pH_{PZSE} and *IEP* are plotted vs. values of $\log K^{\theta}_{L^-} - \log K^{\theta}_{M^+}$ predicted in the present study. The theoretical line is defined by Eqn. (90). Data from Penners et al. (1986) for hematite in KCl ($pH_{PZSE} - IEP$ 0.2; $\log K^{\theta}_{L^-} - \log K^{\theta}_{M^+} = -0.6$) and Rosenqvist et al. (2002) for gibbsite in NaCl ($pH_{PZSE} - IEP = 1.0$; $\log K^{\theta}_{L^-} - \log K^{\theta}_{M^+} = -0.6$) were the only data where both measurements were reported but the result was not consistent with the other data and the theoretical line shown in Figure 11. Reports of no difference between pH_{PZSE} and *IEP* (Sprycha et al., 1989; Rietra et al., 2000; Gunnarsson et al., 2000, 2001; Boily et al., 2001) were also not included in Figure 11 for the sake of clarity. It should be emphasized that substantial uncertainties exist in the experimental and predicted values shown in the figure. Despite the uncertainties, it can be seen in the figure that the experimental values of the difference $pH_{PZSE} - IEP$ range from −0.7 to +0.1 and correlate closely with the theoretical line defined by Eqn. (90).

Figure 11 also includes experimental values of pH_{PZSE} for

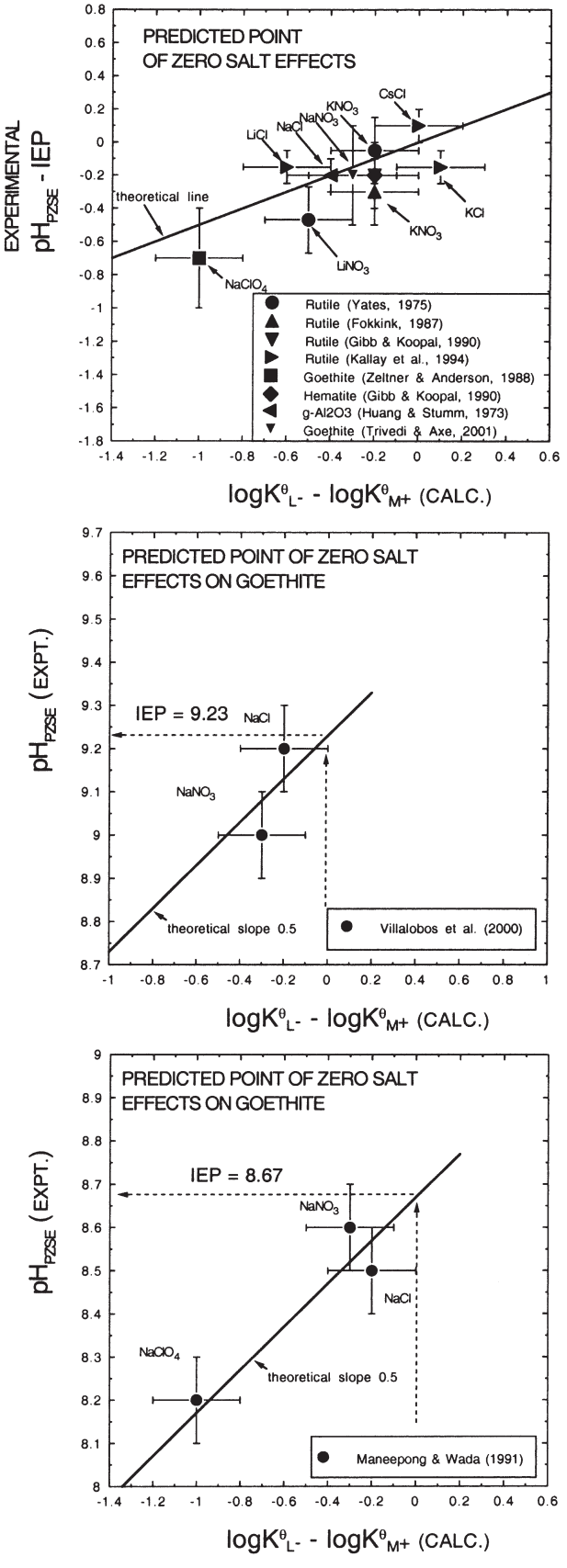

Fig. 11. Experimental values of pH_{PZSE} vs. the differences in the logarithms of the electrolyte anion and cation binding constants ($\log K^{\theta}_{L^-} - \log K^{\theta}_{M^+}$) predicted in the present study. The upper figure refers to experimental values of $pH_{PZSE} - IEP$ from the literature. The solid line represents predicted values of $pH_{PZSE} - IEP = 0.5(\log K^{\theta}_{L^-} - \log K^{\theta}_{M^+})$ using values of the binding constants from Tables 6 and 7. The lower figures represent pH_{PZSE} for samples of goethite in different electrolytes for which the *IEP* has not been measured. The solid lines in these figures have a theoretical slope of 0.5 which enables estimation of the *IEP* values (see text).

samples of goethite in different electrolytes for which the *IEP* has not been measured. Despite the uncertainties in both the abscissa and ordinate values of these points, it can be seen that they are consistent with a rearrangement of Eqn. (90) giving

$$pH_{PZSE} = IEP + 0.5(\log K^{\theta}_{L^-} - \log K^{\theta}_{M^+}) \qquad (91)$$

The solid lines in the figure have the theoretical slope of 0.5, permitting values of the *IEP* to be deduced. Furthermore, the order of anion binding on goethite is predicted to decrease in the sequence Cl^-, NO_3^-, ClO_4^- which is consistent with experimental results (Maneepong and Wada, 1991; Rietra et al., 2000; Villalobos and Leckie, 2001). As a result, it might be expected that the experimental pH_{PZSE} in the Na-electrolyte with the weakest anion would be closest to the *IEP* (Villalobos and Leckie, 2001). However, it can be seen in the two goethite figures that just the opposite is the case. In fact, Na^+ is predicted to bind more strongly to goethite than any of these three anions, therefore the assymetry of binding ($\log K^{\theta}_{L^-} - \log K^{\theta}_{M^+}$ increases in the sequence $NaCl$ (−0.2), $NaNO_3$ (−0.3), $NaClO_4$ (−0.5). It is in $NaCl$ (with the smallest assymetry of binding) that the goethite has a pH_{PZSE} value closest to the *IEP*.

The consistency of the theoretically predicted equilibrium constant differences ($\log K^{\theta}_{L^-} - \log K^{\theta}_{M^+}$ with the measurements plotted in Figure 11 strongly suggests that the difference $pH_{PZSE} - IEP$ can be reliably predicted with Eqn. (90) and Tables 6 and 7. Given the wide range of electrolyte types covered by the combination of Tables 6 and 7, substantial ranges of pH_{PZSE} for a given solid can be expected. For example, the pH_{PZSE} for rutile can be expected to range from about 0.4 above the *IEP* in *NaI* to about 0.6 below the *IEP* in $LiClO_4$. Such ranges can be expected to account for a substantial part of the apparent variation in "zero points of charge" determined from the intersection points of titration curves reported in the literature.

When electrokinetic data are not available, the results above suggest that the *IEP* can be estimated using

$$IEP = pH_{PZSE} - 0.5(\log K^{\theta}_{L^-} - \log K^{\theta}_{M^+}) \qquad (92)$$

and the results in Tables 6 and 7. The result should be useful as a close estimate of the (pristine) point-of-zero charge that can be used to enter a value of pH_{ZPC} into the predictive Eqns. (67) and (80) discussed above.

5. CONCLUDING REMARKS

Combination of the results of analysis of proton surface charge data from previous studies (Criscenti and Sverjensky, 1999; Sahai and Sverjensky, 1997a; Sverjensky, 2001) together with the results of analysis of additional data in the present study (Appendix) has yielded 55 sets of triple-layer parameters referring to wide ranges of ionic strengths and electrolyte types. In terms of the type of solid and the number of parameter sets for that type, the study includes α-TiO_2 (9), β-TiO_2 (3), α-FeOOH (10), α-Fe_2O_3 (14), α-Al_2O_3 (1), γ-Al_2O_3 (2), α-$Al(OH)_3$ (2), α-SiO_2 (3), and amorphous SiO_2 (12). Interpretation and correlation of the parameters with the aid of crystal chemical, electrostatic, and thermodynamic theory permits the following generalizations:

(1) Differences in the surface protonation equilibrium constants pH_{ZPC} and ΔpK^{θ}_n between different solids can be explained using solvation and crystal chemical theory (as previously noted, Sverjensky and Sahai, 1996). That this can be done when the principal parameters used in the theory refer to properties of the bulk solid suggests that the bonding involved in surface species is more analogous to that in solids than in aqueous solutions. The theory enables prediction of values of the pH_{ZPC} and ΔpK^{θ}_n which reduces the number of triple-layer parameters, a matter of some concern in many studies (e.g., Koopal et al., 1987; Hayes et al., 1991; Venema et al., 1996; Lützenkirchen, 1998; Lützenkirchen and Magnico, 1998; Boily et al., 2001). It should be noted that the theoretical values of pH_{ZPC} predicted here are based on the zero point of charge defined by isoelectric points or point-of-zero-salt effects referring to the lowest ionic strengths.

(2) Implementation of new standard states for surface sites and species (Sverjensky, 2003) redefines the equilibrium constants for electrolyte adsorption, now denoted $K^{\theta}_{M^+}$ and $K^{\theta}_{L^-}$. The values of these equilibrium constants can readily be calculated (Eqns. 35 and 36, or 51 and 52) by correcting values of $^*K^{O}_{M^+}$ and $^*K^{O}_{M^+}$ referring to the hypothetical 1.0 M standard state. The practical advantage is that the corrected values $K^{\theta}_{M^+}$ and $K^{\theta}_{L^-}$. no longer depend on the surface areas or site densities of the actual samples. Instead, they are referred to universal values of (hypothetical) standard state site density and surface area defined by $N^{\ddagger} = 10 \times 10^{18}$ sites $\cdot\ m^{-2}$ and $A^{\ddagger} = 10\ m^2 \cdot g^{-1}$. This permits direct comparison of K values for different samples of the same solid, or different solids, with different surface areas or site densities. The magnitude of this correction can be quite large, e.g., amorphous silica samples in Table A1 with BET values of 43 and 380 $m^2 \cdot g^{-1}$ have correction factors that differ by a factor of about 9.

(3) Differences in the values of $K^{\theta}_{M^+}$ and $K^{\theta}_{L^-}$ for different electrolyte ions and solids are accounted for in the present study using crystal chemical and solvation theory, and linear free energy correlations. Predicted trends in $K^{\theta}_{M^+}$ for the alkalis on solids with a wide range of dielectric constants indicate that for high dielectric constant solids (e.g., rutile) the equilibrium constants increase in the sequence Cs^+, Rb^+, K^+, Na^+, Li^+. In contrast, for low dielectric constant solids (e.g., amorphous silica), the predicted sequence is Li^+, Na^+, K^+, Rb^+, Cs^+. Solids with intermediate values of ϵ (e.g., iron and aluminum oxides and hydroxides) have predicted equilibrium constants that are roughly independent of the type of adsorbing alkali cation. This explains why the diffuse double-layer and constant capacitance models for amorphous ferric hydroxide can afford to neglect binding of electrolyte ions.

(4) Point-of-zero-salt effects for surface titration curves can be predicted using the difference $pH_{PZSE} - IEP = 0.5(\log K^{\theta}_{L^-} - \log K^{\theta}_{M^+})$. When the difference between the anion and cation binding is rather small ($|\log K^{\theta}_{L^-} - \log K^{\theta}_{M^+}| \leq 0.6 \rightarrow 0.8$), it can be expected that the titration curves will appear to intersect at essentially a single value (defining a pH_{PZSE}), one that may, however, be noticably different from the *IEP* obtained at low ionic strengths. Consequently, it can be expected that at least

some of the variation reported for "zero points of charge" determined from the intersections of experimental titration curves is attributable to predictable point-of-zero-salt effects. When electrokinetic data are not available, the *IEP* can be estimated from $IEP = pH_{PZSE} + 0.5(\log K^{\theta}_{L^-} - \log K^{\theta}_{M^+})$.

(5) The inner capacitance in the triple-layer model (C_1) is a predictable parameter using crystallographic or hydrated radii (Sverjensky, 2001). On rutile and similar high-dielectric constant solids, the alkali cations adsorb close to the surface as inner-sphere complexes at distances which differ according to the crystallographic cation radii. On most other oxides they adsorb further away as outer-sphere complexes at distances which differ according to hydrated cation radii. With the additional C_1 values of the present study, it has become clear that the model can be used to make separate predictions for the C_1's of DeGussa silicas relative to Cabosil and other silicas. These predictions replace the ones published previously for amorphous silica. The model results suggest that alkali cations are further from the surface on DeGussa silicas relative to other silicas. Similarly, separate predictions of C_1 can now be made for hematites with pH_{PZSE} values 8.4–8.6 relative to hematites with pH_{PZSE} values 9.0–9.5. The latter represent hematites that have been extensively cleaned, which appears to result in surfaces that the alkali cations can approach very closely. In contrast, the C_1 values of the goethite–water interface do not appear to be consistent with a radius-based model. Instead, the C_1 values for goethite in Na-salts follow an empirical correlation with BET surface area.

(6) The outer capacitance in the triple-layer model can be estimated by taking $C_2 = C_1$. This results in reasonable predicted values of the zeta potential (calculated assuming $\zeta = \psi_d$) at pH values within about 2 units of the isoelectric point. The predicted values of C_2 imply model distances between the β-plane and the d-plane of the order of 4 to 7 Å for rutile in LiCl and CsCl, respectively (assuming the dielectric constant of water between the planes is 78). These distances are consistent with total distances of about 7 and 11 Å, respectively, from the surface to the d-plane, where it is assumed that the properties of bulk water obtain.

(7) All the parameters in the triple-layer model can now be estimated with the revised equations presented in this study. It should be emphasized that the predicted parameters refer only to the single-site, 2pK, triple-layer model adopted here. The estimation procedure developed here is consistent with a large body of experimental data on many individual solids and electrolytes. Proton surface charge can be predicted for any oxide in 1:1 electrolyte solutions independent of experiments. Assymetric binding of electrolyte ions is built into these predictions. Such predictions can serve as a complement to the experimental study of new systems, as well as a means of estimation of the role of proton surface charge development in more complex systems, e.g., involving silicates, where additional mechanisms of charge development are likely.

Acknowledgments—This work represents the outgrowth of discussions and previous collaborations with L. J. Criscenti, C. M. Koretsky, and N. Sahai. Discussions with and data provided by J.-F. Boily, J. A. Davis, M. Gunnarsson, K. Hayes, P. Joó, N. Kallay, D. Kulik, R. Kretzschmar, M. Machesky, N. Marmier, W. Piasceki, W. Rudzinski, D. Wesolowski, P. Venema, and M. Villalobos are greatly appreciated. Comments by D. Kulik, M. Machesky, and two anonymous reviewers helped clarify the manuscript considerably. Financial support was provided by DOE Grant DE-FG02-96ER-14616 and DuPont.

Associate editor: M. L. Machesky

REFERENCES

Abendroth R. P. (1970) Behavior of a pyrogenic silica in simple electrolytes. *J. Colloid Interface Sci.* **34** (*4*), 591–596.

Ali M. A (1994) The influence of simple organic acids on sorption of inorganic ions at the goethite/water interface. Ph.D. thesis, University of Pittsburgh.

Baes C. F. and Mesmer R. E. (1976) *The Hydrolysis of Cations*. John Wiley and Sons, Inc.., 489 pp.

Bérubé, Y. G. (1967) Adsorption of inorganic ions at the titanium oxide-solution interface. Ph.D. thesis. Massachusetts Institute of Technology. 161 pp.

Bérubé Y. G. and Bruyn P. L. d. (1968b) Adsorption at the rutile–solution interface II. Model of the electrochemical double layer. *J. Colloid Interface Sci.* **28,** 92–105.

Blesa M. A., Figliolia N. M., Maroto A. J. G. and Regazzoni A. E. (1984) The influence of temperature on the interface magnetite-aqueous electrolyte solution. *J. Colloid Interface Sci.* **101,** 410–418.

Boily J.-F., Lützenkirchen J., Balmès O., Beattie J., and Sjöberg S. (2001) Modeling proton binding at the goethite(α-FeOOH)–water interface. *J. Colloid Interface Sci.* **179,** 11–27.

Bolt G. H. (1957) Determination of the charge density of silica sols. *J. Phys. Chem.* **61,** 1166–1169.

Bourikas K., Hiemstra T., and Riemsdijk W. H. V. (2001) Ion pair formation and primary charging behavior of titanium oxide (anatase and rutile). *Langmuir* **17,** 749–756.

Breeusma A (1973) Adsorption of ions on hematite (Fe_2O_3). Ph.D. thesis, Agricultural University, Netherlands.

Carroll-Webb S. A. and Walther J. V. (1988) A surface complex reaction model for the pH-dependencies of corundum and kaolinite dissolution rates. *Geochim. Cosmochim. Acta* **52,** 2609–2623.

Casey W. H. (1994) Enthalpy changes for Bronsted acid-base reactions on silica. *J. Colloid Interface Sci.* **163,** 407–419.

Christl I. and Kretzschmar R. (1999) Competitive sorption of copper and lead at the oxide–water interface: Implications for surface site density. *Geochim. Cosmochim. Acta* **63,** 2929–2938.

Criscenti L. J. and Sverjensky D. A. (1999) The role of electrolyte anions ClO_4^-, NO_3^-, and Cl^- in divalent metal (M^{2+}) adsorption on oxide and hydroxide surfaces in salt solutions. *Am. J. Sci.* **299,** 828–899.

Criscenti L. J. and Sverjensky D. A. (2002) A single-site model for divalent and heavy metal adsorption over a range of metal concentrations. *J. Colloid Interface Sci.* **253,** 329–352.

Csobän K. and Joó P. (1999) Sorption of Cr(III) on silica and aluminum oxide: Experiments and modelling. *Colloids and Surfaces* **151,** 97–112.

Davis J. A., James R. O., and Leckie J. O. (1978) Surface ionization and complexation at the oxide/water interface I. Computation of electrical double layer properties in simple electrolytes. *J. Colloid Interface Sci.* **63,** 480–499.

Davis J. A. and Leckie J. O. (1978) Surface ionization and complexation at the oxide/water interface II. Surface properties of amorphous iron oxyhydroxide and adsorption of metal ions. *J. Colloid Interface Sci.* **67,** 90–107.

Davis J. A. and Kent D. B. (1990) Surface complexation modeling in aqueous geochemistry. In *Mineral–Water Interface Geochemistry*, Vol. 23 (eds. M. F. Hochella, Jr. and A. F. White), pp. 177–259. Mineralogical Society of America.

Drever J. I. (1997) *The Geochemistry of Natural Waters*, 3rd ed Prentice Hall, 436 pp.

Dugger D. L., Stanton J. H., Irby B. N., McConnell B. L., Cummings W. W., and Maatman R. W. (1964) The exchange of twenty metal ions with the weakly acidic silanol group of silica gel. *J. Phys. Chem.* **68,** 757–760.

Dzombak D. A. and Morel F. M. M. (1990) *Surface Complexation Modeling*. John Wiley and Sons.

Felmy A. R. and Rustad J. R. (1998) Molecular statics calculations of proton binding to goethite surfaces: Thermodynamic modeling of the surface charging and protonation of goethite in aqueous solution. *Geochim. Cosmochim. Acta* **62,** 25–31.

Fenter P., Cheng L., Rihs S., Machesky M., Bedyzk M. D., and Sturchio N. C. (2000) Electrical double-layer structure at the rutile–water interface as observed *in situ* with small-period X-ray standing waves. *J. Colloid Interface Sci.* **225,** 154–165.

Fokkink L. G. J (1987) Ion adsorption on oxides: Surface charge and cadmium binding on rutile and hematite. Ph.D. thesis, Wageningen.

Geelhoed J. S., Hiemstra T., and van Riemsdijk W. H. (1997) Phosphate and sulfate adsorption on goethite: Single anion and competitive adsorption. *Geochim. Cosmochim. Acta* **61,** 2389–2396.

Gibb A. W. M. and Koopal L. K. (1990) Electrochemistry of a model for patchwise heterogeneous surfaces: The rutile–hematite system. *J. Colloid Interface Sci.* **134,** 122–138.

Goloub T. P., Koopal L. K., and Bijsterbosch B. H. (1996) Adsorption of cationic surfactants on silica: Surface charge effects. *Langmuir* **12,** 3188–3194.

Gunnarsson M., Jakobsson A., Ekberg S., Albinson Y., and Ahlberg E. (2000) Sorption studies of cobalt (II) on colloidal hematite using potentiometry and radioactive tracer technique. *J. Colloid Interface Sci.* **231,** 326–336.

Gunnarsson M., Rasmusson M., Wall S., Ahlberg E., and Ennis J. (2001) Electroacoustic and potentiometric studies of the hematite/water interface. *J. Colloid Interface Sci.* **240,** 448–458.

Hayes K. F (1987) Equilibrium, spectroscopic, and kinetic studies of ion adsorption at the oxide–aqueous interface. Ph.D. thesis, Stanford University, 260 pp.

Hayes K. F., Redden G., Ela W., and Leckie J. O. (1991) Surface complexation models: An evaluation of model parameter estimation using FITEQL and oxide mineral titration data. *J. Colloid Interface Sci.* **142,** 448–469.

Helgeson H. C. and Kirkham D. H. (1976) Theoretical prediction of the thermodynamic properties of aqueous electrolytes at high pressures and temperatures. III. Equation of state for aqueous species at infinite dilution. *Am. J. Sci.* **276,** 97–240.

Hiemstra T., van Riemsdijk W. H., and Bruggenwert M. G. (1987) Proton adsorption mechanism at the gibbsite and aluminum oxide solid/solution interface. *Netherlands Journal of Agricultural Science* **35,** 281–293.

Hiemstra T., van Riemsdijk W. H., and Bolt G. H. (1989a) Multisite proton adsorption modeling at the solid/solution interface of (hydr)oxides: A new approach I. Model description and evaluation reaction constants. *J. Colloid Interface Sci.* **133** (*1*), 91–104.

Hiemstra T., Wit J. C. M. D., and van Riemsdijk W. H. (1989b) Multisite proton adsorption modeling at the solid/solution interface of (hydr)oxides: A new approach II. Applications to various important (hydr)oxides. *J. Colloid Interface Sci.* **133** (*1*), 105–117.

Hiemstra T. and van Riemsdijk W. H. (1990) Multiple activated complex dissolution of metal (hydr)oxides: A thermodynamic approach applied to quartz. *J. Colloid Interface Sci.* **136** (*1*), 132–150.

Hiemstra T. and van Riemsdijk W. H. (1996) A surface structural approach to ion adsorption: The charge distribution (CD) model. *J. Colloid Interface Sci.* **179,** 488–508.

Hiemstra T. and van Riemsdijk W. H. (2000) Fluoride adsorption on goethite in relation to different types of surface sites. *J. Colloid Interface Sci.* **225,** 94–104.

Huang C. and Stumm W. (1973) Specific Adsorption of Cations on Hydrous g-Al_2O_3. *J. Colloid Interface Sci.* **43** (*2*), 409–420.

Huang P (1996) The effects of the adsorption of metal ions and surfactant behavior on the interfacial behavior of silicate minerals. Ph.D. thesis, University of California, Berkeley.

Hunter R. J. (1986) *Foundations of Colloid Science* Vol. I. Oxford University Press, 670 pp.

Hunter R. J. (1989) *Foundations of Colloid Science* Vol. II. Clarendon Press, 1089 pp.

James R. O. and Healy T. W. (1972) Adsorption of hydrolyzable metal ions at the oxide–water interface III. A thermodynamic model of adsorption. *J. Colloid Interface Sci.* **40,** 65–81.

James R. O. and Parks G. A. (1982) Characterization of aqueous colloids by their electrical double-layer and intrinsic surface chemical properties. In *Surface and Colloid Science*, Vol. 12 (ed. E. Matijevic), pp. 119–216. Plenum Press.

Johnson S. B., Scales P. J., and Healy T. W. (1999) The binding of monovalent electrolyte ions on α-alumina. I. Electroacoustic studies at high electrolyte concentrations. *Langmuir* **15,** 2836–2843.

Kallay N., Colic M., Fuerstenau D. W., Jang H. M., and Matijevic E. (1994) Lyotropic effect in surface charge, electrokinetics, and coagulation of a rutile dispersion. *Colloid Polymer Sci.* **272,** 554–561.

Karlsson M., Craven C., Dove P. M., and Casey W. H. (2001) Surface charge concentrations on silica in diffferent 1.0 m metal–chloride background electrolytes and implications for dissolution rates. *Aquatic Geochem.* **7,** 13–32.

Koopal L. K., Riemsdijk W. H. v., and Roffey M. G. (1987) Surface ionization and complexation models: A comparison of methods for determining model parameters. *J. Colloid Interface Sci.* **118,** 117–136.

Koretsky C. M., Sverjensky D. A., and Sahai N. (1998) A model of surface site types on oxide and silicate minerals based on crystal chemistry: Implications for site types and densities, multi-site adsorption, surface infrared spectroscopy, and dissolution kinetics. *Am. J. Sci.* **298,** 349–438.

Kosmulski M. (2001) *Chemical Properties of Material Surfaces*. Marcel Dekker. 753 pp.

Kosmulski M. (2002) The pH-dependent surface charging and the points of zero charge. *J. Colloid Interface Sci.* **253,** 77–87.

Kulik D. A. (2000) Thermodynamic properties of surface species at the mineral–water interface under hydrothermal conditions: A Gibbs energy minimization single-site $2pK_A$ triple-layer model of rutile in NaCl electrolyte to 250°C. *Geochim. Cosmochim. Acta* **64,** 3161–3179.

Kulik D. A. (2002) A Gibbs energy minimization approach to model sorption equilibria at the mineral–water interface: Thermodynamic relations for multi-site surface-complexation. *Am. J. Sci.* **302,** 227–279.

Langmuir D. (1997) *Aqueous Environmental Geochemistry*. Prentice-Hall, 600 pp.

Legrand A. P. (1998) *The Surface Properties of Silicas*. John Wiley and Sons, 470 pp.

Liang L (1988) Effects of surface chemistry on kinetics of coagulation of submicron iron oxide particles (α-Fe_2O_3) in water. Ph.D. thesis, California Institute of Technology.

Lövgren L., Sjöberg S., and Schindler P. W. (1990) Acid/base reactions and Al(III) complexation at the surface of goethite. *Geochim. Cosmochim. Acta* **54,** 1301–1306.

Lumsden D. G. and Evans L. J. (1994) Surface complexation model parameters for goethite (α-FeOOH). *J. Colloid Interface Sci.* **164,** 119–125.

Lützenkirchen J. (1998) Parameter estimation for the triple layer model. Analysis of conventional methods and suggestion of alternative possibilities. *J. Colloid Interface Sci.* **204,** 119–127.

Lützenkirchen J. and Magnico P. (1998) Some considerations on the triple layer model framework. *Colloids and Surfaces* **137,** 345–354.

Machesky M., Wesolowski D. J., Palmer D. A., and Ichiro-Hayashi K. (1998) Potentiometric titrations of rutile suspensions to 250°C. *J. Colloid Interface Sci.* **200,** 298–309.

Maneepong S. and Wada S. (1991) Stability of Cl^-, NO_3^-, $ClO4_3^-$, and $SO4_3^{--}$ surface complexes at synthetic goethite/aqueous electrolyte interfaces. *Soil Sci. Plant Nutrition* **37,** 141–150.

Marmier N., Delisée A., and Fromage F. (1999) Surface complexation modeling of Yb(III) and Cs(I) sorption on silica. *J. Colloid Interface Sci.* **212,** 228–233.

McKinley J. P., Zachara J. M., Smith S. C., and Turner G. D. (1995) The influence of uranyl hydrolysis and multiple site-binding reactions on adsorption of U(VI) to montmorillonite. *Clays and Clay Minerals* **43,** 586–598.

Michael H. L. and Williams D. J. A. (1984) Electrochemical properties of quartz. *J. Electroanalyt. Chem.* **179,** 131–139.

Milonji′c S. K. (1987) Determination of surface ionization constants at colloidal silica/electrolyte interface. *Colloids and Surfaces* **23,** 301–312.

Olhoeft G. R. (1981) Electrical properties of rocks. In *Physical Properties of Rocks and Minerals* (ed. Y. S. Touloukian, W. R. Judd, and R. F. Roy), pp. 257–330. McGraw-Hill.

Onoda G. Y. and Bruyn P. L. d. (1966) Proton adsorption at the ferric oxide/aqueous solution interface. *Surface Science* **4,** 48–63.

Papirer E. (2000) Adsorption on silica surfaces. In *Surfactant Science Series*, Vol. 90 (ed. A. T. Hubbard), Marcel Dekker. 753 pp.

Parks, G. A. (1975) Adsorption in the marine environment. In Chemical Oceanography, Vol. 1 (ed. J. P. Riley and G. Skirrow), pp. 241–306. Academic Press.

Penners N. H. G., Koopal L. K., and Lyklema J. (1986) Interfacial electrochemistry of haemite (α-Fe_2O_3): Homodisperse and heterodisperse sols. *Colloids and Surfaces* **21,** 457–468.

Riese A. C (1982) Adsorption of radium and thorium onto quartz and kaolinite: A comparison of solution/surface equilibrium models. Ph.D. thesis, Colorado School of Mines.

Rietra R. P. J. J., Hiemstra T., and van Riemsdijk W. H. (2000) Electrolyte anion affinity and its effect on oxyanion adsorption on goethite. *J. Colloid Interface Sci.* **229,** 199–206.

Robertson A. P (1996) Goethite/humic acid interactions and their effects on copper (II) binding. Ph.D. thesis, Stanford University.

Robertson A. P. and Leckie J. O. (1997) Cation binding predictions of surface complexation models: Effects of pH, ionic strength, cation loading, surface complex, and model fit. *J. Colloid Interface Sci.* **188,** 444–472.

Robinson R. A. and Stokes R. H. (1959) *Electrolyte Solutions*. Butterworths. 571 pp.

Rosenqvist J., Persson P., and Sjöberg S. (2002) Protonation and charging of nanosized gibbsite (α-$Al(OH)_3$) particles in aqueous supension. *Langmuir* **18,** 4598–4604.

Rudzinski W., Charmas R., and Partyka S. (1991) Calorimetric studies of ion adsorption at a water/oxide interface: Effects of energetic heterogeneity of real oxide surfaces. *Langmuir* **7,** 354–362.

Rudzinski W., Charmas R., Partyka S., Thomas F., and Bottero J. Y. (1992) On the nature of the energetic surface heterogeneity in ion adsorption at a water/oxide interface: The behavior of potentiometric, electrokinetic, and radiometric data. *Langmuir* **8,** 1154–1164.

Rudzinski W., Charmas R., Partyka S., and Bottero J. Y. (1993) On the nature of the energetic heterogeneity in ion adsorption at a water/oxide interface: Theoretical studies of some special features of ion adsorption at low ion concentrations. *Langmuir* **9,** 2641–2651.

Rudzinski W., Charmas R., Piasecki W., Thomas F., Villieras F., Prelot B., and Cases J. M. (1998) Calorimetric effects accompanying ion adsorption at the charged metal oxide/electrolyte interfaces: Effects of oxide surface energetic heterogeneity. *Langmuir* **14,** 5210–5225.

Rudzinski W., Piasecki W., Panas G., and Charmas R. (2000) Calorimetric effects and temperature dependence of simple ion adsorption at oxide/electrolyte interfaces: The systems in which PZC and CIP do not coincide. *J. Colloid Interface Sci.* **226,** 353–363.

Rustad J. R., Felmy A. R., and Hay B. P. (1996a) Molecular statics calculations for iron oxide and oxyhydroxide minerals: Toward a flexible model of the reactive mineral–water interface. *Geochim. Cosmochim. Acta* **60,** 1553–1562.

Rustad D. J., Felmy A. R., and Hay B. P. (1996b) Molecular statics calculations of proton binding to goethite surfaces: A new approach to estimation of stability constants for multisite surface complexation models. *Geochim. Cosmochim. Acta* **60,** 1563–1576.

Sahai N. and Sverjensky D. A. (1997a) Evaluation of internally-consistent parameters for the triple-layer model by the systematic analysis of oxide surface titration data. *Geochim. Cosmochim. Acta* **61,** 2801–2826.

Sahai N. and Sverjensky D. A. (1997b) Solvation and electrostatic model for specific electrolyte adsorption. *Geochim. Cosmochim. Acta* **61,** 2827–2848.

Schindler P. W. and Stumm W. (1987) The surface chemistry of oxides, hydroxides, and oxide minerals. In Aquatic Surface Chemistry: Chemical Processes at the Particle–Water Interface (ed. W. Stumm), pp. 83–110. John Wiley and Sons.

Schudel M., Behrens S. H., Holthoff H., Kretzschmar R., and Borkovec M. (1997) Absolute aggregation rate constants of hematite particles in aqueous suspensions: A comparison of two different surface morphologies. *J. Colloid Interface Sci.* **196,** 241–253.

Shannon R. D. and Prewitt C. T. (1969) Effective ionic radii in oxides and fluorides. *Acta. Cryst.* **B25,** 925–946.

Shannon R. D. (1993) Dialectic polarizabilities of ions in oxides and fluorides. *J. Appl. Phys.* **73,** 348–366.

Shannon R. D., Iishi K., Allik T. H., Rossman G. R., and Liebertz J. (1992) Dialectric constants of BaO and melilites and the oxide additivity rule. *European Journal of Minerology* **4,** 1241–1249.

Shock E. L. and Helgeson H. C. (1988) Calculation of the thermodynamic and transport properties of aqueous species at high pressures and temperatures correlation algorithms for ionic aqueous species and equation of state predictions to 5 kb and 1000 C. *Geochim. Cosmochim. Acta* **52,** 2009–2036.

Shock E. L., Helgeson H. C., and Sverjensky D. A. (1989) Calculation of the thermodynamic and transport properties of aqueous species at high pressures and temperatures: Standard partial molal properties of inorganic neutral species. *Geochim. Cosmochim. Acta* **53,** 2157–2184.

Shock E. L., Sassani D. C., Willis M., and Sverjensky D. A. (1997) Inorganic species in geologic fluids: Correlations among standard molal thermodynamic properties of aqueous cations, oxyanions, acid oxyanions, oxyacids and hydroxide complexes. *Geochim. Cosmochim. Acta* **61,** 907–950.

Skinner B. J. (1979) The many origins of hydrothermal ore deposits. In *Geochemistry of Hydrothermal Ore Deposits* (ed. H. L. Barnes), pp. 1–21. Holt, Rinehart and Winston.

Smyth J. R. and Bish D. L. (1988) *Crystal Structures and Cation Sites of the Rock-Forming Minerals*. Allen & Unwin.

Sonnefeld J. (2001) On the influence of background electrolyte concentration on the position of the isoelectric point and the point of zero charge. *Colloids and Surfaces* **190,** 179–183.

Sonnefeld J., Göbel A., and Vogelsberger W. (1995) Surface charge density on spherical silica particles in aqueous alkali chloride solutions. *Colloid Polymer Sci.* **273,** 926–931.

Sonnefeld J., Löbbus M., and Vogelsberger W. (2001) Determination of electric double layer parameters for spherical silica particles under application of the triple-layer model using surface charge density data and results of electrokinetic sonic amplitude measurements. *Colloids and Surfaces* **195,** 215–225.

Sposito G. (1984) *The Surface Chemistry of Soils*. Oxford University Press. 234 p.

Sposito G. (1998) On points of zero charge. *Environ. Sci. Technol.* **32,** 2815–2819.

Sprycha R. (1984) Surface charge and adsorption of background electrolyte ions at anatase/electrolyte interface. *J. Colloid Interface Sci.* **102,** 173–185.

Sprycha R. (1989) Electrical double layer at alumina/electrolyte interface: I. Surface charge and zeta potential. *J. Colloid Interface Sci.* **127,** 1–11.

Sprycha R. and Sprycha J. (1984) Estimation of surface ionization constants from electrokinetic data. *J. Colloid Interface Sci.* **102,** 288–291.

Stumm W. (1992) *Chemistry of the Solid–Water Interface*. John Wiley and Sons, 428 pp.

Sverjensky D. A., Hemley J. J., and D'Angelo W. M. (1991) Thermodynamic assessment of hydrothermal alkali feldspar-mica-aluminosilicate equilibria. *Geochim. Cosmochim. Acta* **55,** 989–1004.

Sverjensky D. A. (1993) Physical surface-complexation models for sorption at the mineral–water interface. *Nature* **364** (August 26), 776–780.

Sverjensky D. A. (1994) Zero-point-of-charge prediction from crystal chemistry and solvation theory. *Geochim. Cosmochim. Acta* **58,** 3123–3129.

Sverjensky D. A. (2001) Interpretation and prediction of triple-layer model capacitances and the structure of the oxide–electrolyte–water interface. *Geochim. Cosmochim. Acta* **65,** 3641–3653.

Sverjensky D. A. (2003) Standard states for the activities of mineral surface-sites and species. *Geochim. Cosmochim. Acta* **67,** 17–28.

Sverjensky D. A. and Sahai N. (1996) Theoretical prediction of single-site surface protonation equilibrium constants for oxides and silicates in water. *Geochim. Cosmochim. Acta* **60,** 3773–3798.

Tadros T. F. and Lyklema J. (1968) Adsorption of potential-determining ions at the silica–aqueous electrolyte interface and the role of some cations. *Electroanalyt. Chem. Interfac. Electrochem.* **17,** 267–275.

Trivedi P. and Axe L. (2001) Ni and Zn sorption to amorphous versus crystalline iron oxides: Macroscopic studies. *J. Colloid Interface Sci.* **244,** 221–229.

Van Geen A., Robertson A. P., and Leckie J. O. (1994) Complexation of carbonate species at the goethite surface: Implications for adsorption of metal ions in natural waters. *Geochim. Cosmochim. Acta* **58,** 2073–2086.

Venema P., Hiemstra T., and van Riemsdijk W. H. (1996) Comparison of different site-binding models for cation sorption: Description of pH dependency, salt dependency, and cation-proton exchange. *J. Colloid Interface Sci.* **181,** 45–59.

Venema P., Hiemstra T., and van Riemsdijk W. H. (1997) Interaction of cadmium with phosphate on goethite. *J. Colloid Interface Sci.* **192,** 94–103.

Villalobos M. and Leckie J. O. (2001) Surface complexation modeling and FTIR study of carbonate adsorption to goethite. *J. Colloid Interface Sci.* **235,** 15–32.

Weerasooriya R., Aluthpatabendi D., and Tobschall H. J. (2001) Charge distribution multi-site (CD-MUSIC) modeling of Pb(II) adsorption on gibbsite. *Colloids and Surfaces* **189,** 131–144.

Weidler P. G., Degovics G., and Laggner P. (1998) Surface roughness created by acidic dissolution of synthetic goethite monitored with SAXS and N_2-adsorption isotherms. *J. Colloid Interface Sci.* **197,** 1–8.

Yates D. E (1975) The structure of the oxide/aqueous electrolyte interface. Ph.D. thesis, University of Melbourne.

Yoon R. H., Salman T., and Donnay G. (1979) Predicting points of zero charge of oxides and hydroxides. *J. Colloid Interface Sci.* **70,** 483–493.

Zeltner W. A. and Anderson M. A. (1988) Surface charge development at the goethite/aqueous solution interface: Effects of CO_2 adsorption. *Langmuir* **4,** 469–474.

Zhang Z, Fenter P, Cheng L, Sturchio N. C, Bedyzk M. D, Predota M, Bandura A. V, Kubicki J. D, Lvov S. N, Cummings P. T, Chialvo A. A, Ridley M. K, Benezeth P, Anovitz L, Palmer D. A, Machesky M., and, Wesolowski D. J (2004) Ion adsorption at the rutile–water interface: Linking molecular and macroscopic properties. (*Langmuir* **20,**4954-4969.

Zuyi T. and Hongxia Z. (2002) Acidity and alkali metal adsorption on the SiO_2–aqueous solution interface. *J. Colloid Interface Sci.* **252,** 15–20.

APPENDIX

The Appendix Figures A1–A3. contain plots of experimental proton surface charge data as functions of pH and ionic strength from a wide array of surface charge studies (Bolt, 1957; Bérubé and Bruyn, 1968; Abendroth, 1970; Breeusma, 1973; Huang and Stumm, 1973; Yates, 1975; Riese, 1982; Michael and Williams, 1984; Sprycha and Sprycha, 1984; Penners et al., 1986; Fokkink, 1987; Hayes, 1987; Milonji′c, 1987; Liang, 1988; Sprycha, 1989; Gibb and Koopal, 1990; Hayes et al., 1991; Ali, 1994; Casey, 1994; Kallay et al., 1994; Lumsden and Evans, 1994; Van Geen et al., 1994; Goloub et al., 1996; Huang, 1996; Robertson, 1996; Venema et al., 1996; Robertson and Leckie, 1997; Schudel et al., 1997; Machesky et al., 1998; Christl and Kretzschmar, 1999; Csobän and Joó, 1999; Marmier et al., 1999; Gunnarsson et al., 2000; Boily et al., 2001; Gunnarsson et al., 2001; Sonnefeld et al., 2001; Villalobos and Leckie, 2001; Weerasooriya et al., 2001). The solid curves in the figures represent calculations carried out in the present study using the parameters in Table A1 and the extended triple-layer approach described previously (Sahai and Sverjensky, 1997a; Criscenti and Sverjensky, 1999; Sverjensky, 2001; Criscenti and Sverjensky, 2002). In this approach, the fitted parameters are the capacitance (C_1) and the equilibrium constants of the electrolyte cation ($\log^* K^{\theta}_{M^+}$) and anion ($\log^* K^{\theta}_{L^-}$). These equilibrium constants refer to the hypothetical 1.0 M standard state.

All other parameters for these systems (Table A1) were estimated in a manner consistent with the extended triple-layer approach. The site densities (N_s) were taken from Sahai and Sverjensky (1997a,b) and Criscenti and Sverjensky (1999) and are consistent with the results of tritium exchange experiments and the estimations made from crystal structure considerations (Koretsky et al., 1998). The pH_{ZPC} values are isoelectric points at low ionic strengths where these were available. In other instances, the point-of-zero-salt effect referring to the lowest ionic strengths available was used (see footnotes to the table). For most amorphous silicas, the theoretical $pH_{ZPC} = 2.8$ (Table 5) was used. The values of the surface protonation equilibrium constants $\log K^{\theta}_1$ and $\log K^{\theta}_2$ in Table A1 were calculated from the given pH_{ZPC} values and theoretical values of ΔpK^{θ}_n from Table 5.

It can be seen in Figures A1–A3 that in most instances the solid curves are within about $\pm 2\ \mu C \cdot cm^{-2}$. However, for most of the silicas at pH > 9, the calculated curves are systematically too high compared with the data, particularly at the highest ionic strengths. The reason for this discrepancy is not clear. At pH values more than 6 units above the pH_{ZPC}, it is possible that the assumption that the sorbate species obey Henry's Law is no longer valid. If so, surface activity coefficient effects could be responsible for the systematic departures of the calculated curves from the experimental data. However, it is also true that at high pH values and ionic strengths, the experimentally derived datapoints become inceasingly sensitive to assumptions made regarding aqueous phase activity coefficients as well as corrections for the presence of soluble aqueous silica species.

One plot in Figure A2 does not consist of surface charge data. Instead, the data refer to the adsorption of Cs onto silica in the presence of a 0.01 and 0.1 M $NaNO_3$ solution (Marmier et al., 1999). Adequate fits to the 0.01 M data were obtained with the usual type of surface species ($>SO^-\_Cs^+$). However, at the higher ionic strength of 0.1 M, the species $>SO^-\_CsOH^0$ was necessary.

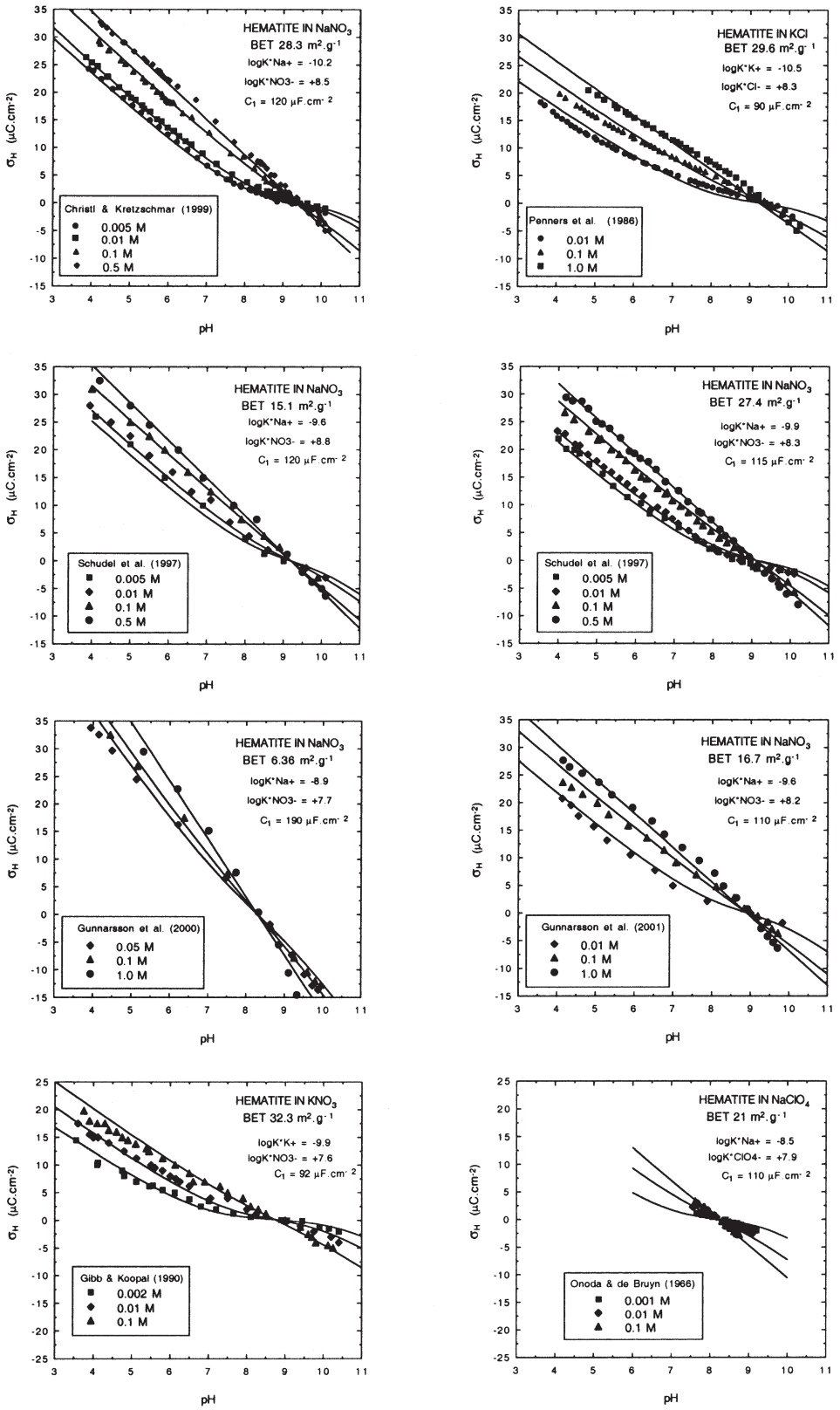

Fig. A1. Plots of proton surface charge as functions of pH and ionic strength for hematite in electrolyte solutions. The symbols represent experimental data. The curves were generated by regression in the present study to obtain values of the capacitance (C_1) and the equilibrium constants of the electrolyte cation ($\log^* K^0_{M^+}$) and anion ($\log^* K^0_{L^-}$) as described in the text.

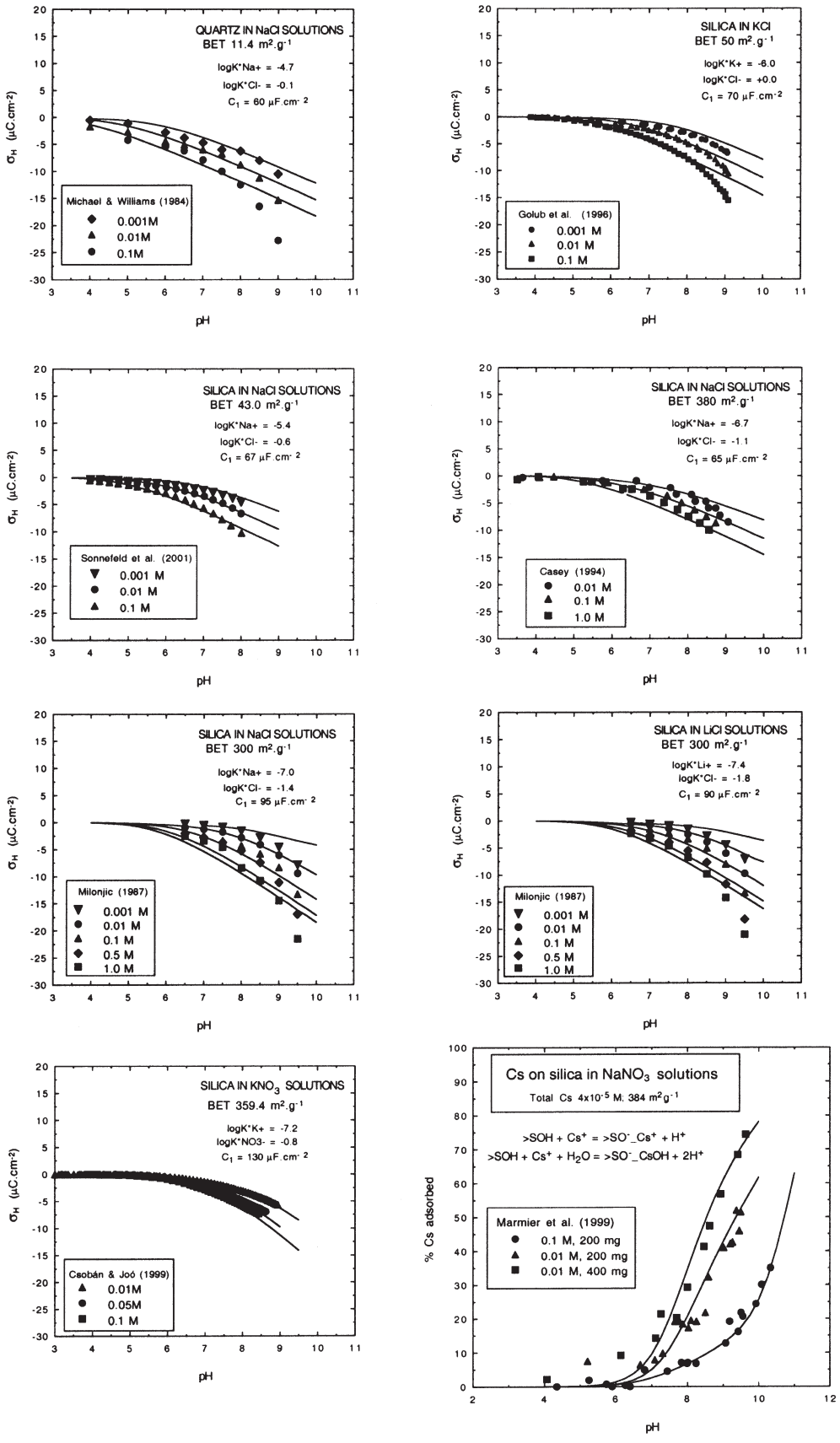

Fig. A2. Plots of proton surface charge and amount adsorbed as functions of pH and ionic strength for quartz and amorphous silica in electrolyte solutions. The symbols represent experimental data. The curves were generated by regression in the present study to obtain values of the capacitance (C_1) and the equilibrium constants of the electrolyte cation ($\log^* K^0_{M^-}$) and anion ($\log^* K^0_{L^-}$) as described in the text.

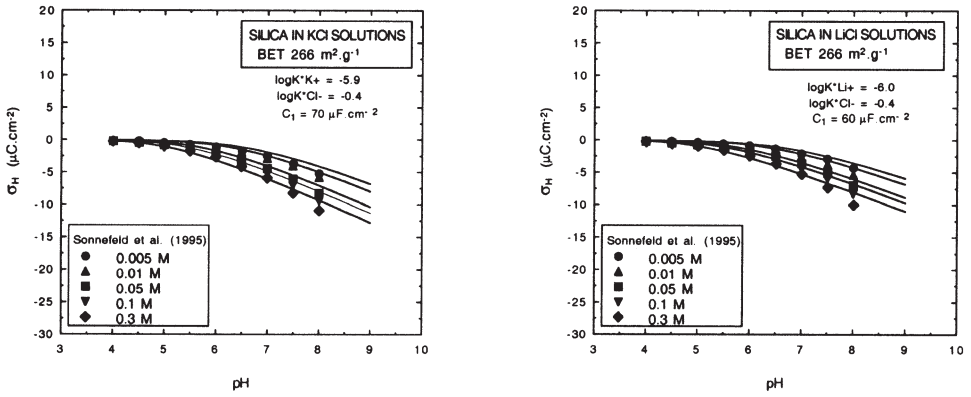

Fig. A2. (Continued)

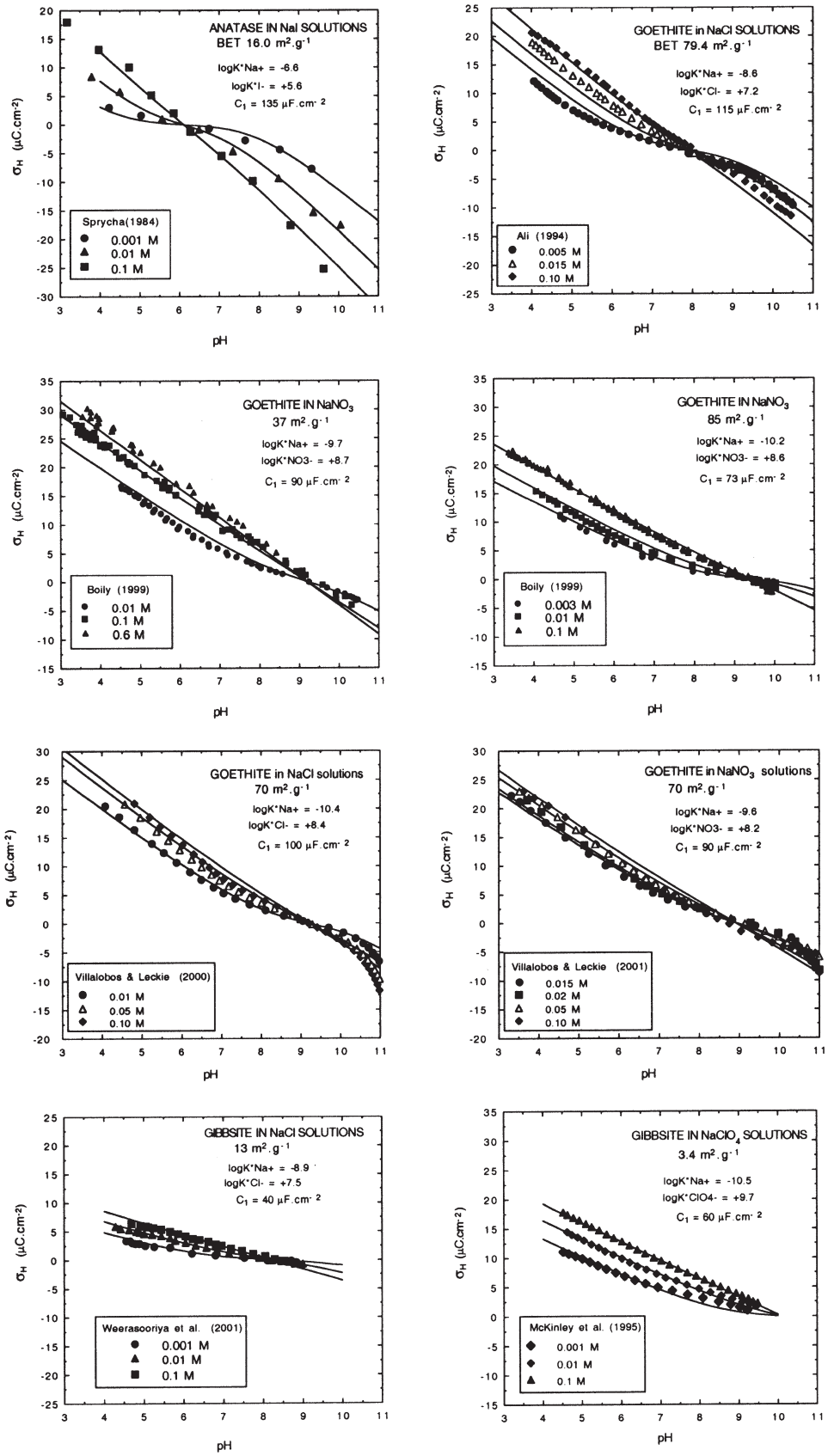

Fig. A3. Plots of proton surface charge as functions of pH and ionic strength for anatase, goethite, and gibbsite unelectrolyte solutions. The symbols represent experimental data. The curves were generated by regression in the present study to obtain values of the capacitance (C_1) and the equilibrium constants of the electrolyte cation ($\log^* K^0_{M-}$) and anion ($\log^* K^0_{L-}$) as described in the text.

Table A1. Triple-layer model parameters $\log^*K^0_{M^+}$, $\log^*K^0_{L^-}$, and C_1 derived from regression of surface-charge experiments referring to wide ranges of ionic strength. Values of $\log K^\theta_{M^+}$ and $\log K^\theta_{L^-}$ were calculated from the regression values of $\log^*K^0_{M^+}$ and $\log^*K^0_{L^-}$ and the tabulated values of N_s, A_s, pH_{ZPC} and ΔpK^θ_n with the aid of Eqns. (51) and (52). Values of $\log K^\theta_1$ and $\log K^\theta_2$ were calculated from the values of pH_{ZPC} and ΔpK^θ_n with the aid of Eqns. (11) and (12). The pH_{ZPC} values are isoelectric points taken from the references cited for the surface charge data unless otherwise noted. The ΔpK^θ_n values are from Table 5. The site densities (N_s) are estimates (see text) unless otherwise noted.

Solid	Salt (ML)	N_s sites · nm^{-2}	A_s m^2 · g^{-1}	pH_{ZPC}	ΔpK^θ_n	$\log K^\theta_1$	$\log K^\theta_2$	$\log^*K^0_{M^+}$	$\log^*K^0_{L^-}$	C_1 μF · cm^{-2}	$\log K^\theta_{M^+}$	$\log K^\theta_{L^-}$	Source of the surface charge data
α-TiO_2	LiCl	12.5	21.0	6.0	6.3	2.8	9.2	−6.4	5.0	155	3.2	2.6	Kallay et al. (1994)[a]
α-TiO_2	$LiNO_3$	12.5[f]	20.0	5.8	6.3	2.7	9.1	−7.1	4.8	145	2.3	2.6	Yates (1975)[b]
α-TiO_2	NaCl	12.5	17.0	5.4[g]	6.3	2.2	8.6	−6.1	4.5	120	2.8	2.6	Machesky et al. (1998)[a]
α-TiO_2	$NaNO_3$	12.5	43.0	6.2[h]	6.3	2.6	9.0	−6.7	5.0	130	3.4	2.7	Bérubé and de Bruyn (1968a)[b]
α-TiO_2	$NaClO_4$	12.5	43.0	6.2[h]	6.3	2.8	9.2	−7.0	4.4	125	3.1	2.5	Bérubé and de Bruyn (1968b)[a]
α-TiO_2	KNO_3	12.5	51.0	5.9	6.3	2.3	8.7	−6.2	4.8	125	3.7	2.9	Fokkink (1987)[b]
α-TiO_2	KNO_3	12.5[f]	20.0	5.8	6.3	2.6	9.0	−6.9	4.8	110	2.5	2.6	Yates (1975)[a]
α-TiO_2	CsCl	12.5	21.0	6.0	6.3	2.8	9.2	−6.7	5.2	95	2.9	2.8	Kallay et al. (1994)[a]
α-TiO_2	$N(CH_3)_4Cl$	12.5[f]	20.0	5.8	6.3	2.6	9.0	−5.6	6.0	55	3.8	3.7	Yates (1975)[a]
β-TiO_2	LiCl	12.5	16.0	6.0	6.4	2.8	9.2	−6.0	5.9	140	3.5	3.4	Sprycha (1984)[b]
β-TiO_2	NaCl	12.5	16.0	6.0	6.4	2.8	9.2	−6.3	5.7	130	3.2	3.2	Sprycha (1984)[b]
β-TiO_2	NaI	12.5	16.0	6.0	6.4	2.8	9.2	−6.6	5.6	135	2.9	3.3	Sprycha (1984)[a]
α-FeOOH	NaCl	16.4	79.4	8.0[i]	5.6	5.2	10.8	−8.6	7.2	115	3.3	3.1	Ali (1994)[e]
α-FeOOH	NaCl	16.4	86.0	9.1[j]	5.6	6.3	11.9	−9.5	8.7	60	3.6	3.6	Lumsden and Evans (1994)[b]
α-FeOOH	NaCl	16.4	70.0	9.2[k]	5.6	6.4	12.0	−10.0	8.4	100	3.1	3.1	Villalobos and Leckie (2001)[e]
α-FeOOH	$NaNO_3$	16.4	37.0	9.4	5.6	6.6	12.2	−9.7	8.7	90	3.3	2.9	Boily et al. (2001)[e]
α-FeOOH	$NaNO_3$	16.4	52.0	8.4	5.6	5.6	11.2	−9.0	8.0	60	3.2	3.3	Hayes (1987)[c]
α-FeOOH	$NaNO_3$	16.4	70.0	9.2[k]	5.6	6.2	11.8	−9.6	8.2	90	3.5	2.9	Villalobos and Leckie (2001)[e]
α-FeOOH	$NaNO_3$	16.4	85.0	9.4	5.6	6.6	12.2	−10.2	8.6	73	3.1	3.1	Boily et al. (2001)[e]
α-FeOOH	$NaNO_3$	16.4	95.0	9.3[l]	5.6	6.5	12.1	−9.8	8.5	60	3.5	3.2	Venema et al. (1996)[d]
α-FeOOH	$NaClO_4$	16.4	49.0	9.2[k]	5.6	6.1	11.7	−9.2	8.0	120	3.7	2.8	Robertson (1996)[d]
α-FeOOH	$NaClO_4$	16.4	45.0	9.2[k]	5.6	6.1	11.7	−9.5	7.8	145	3.4	2.6	Van Geen et al. (1994)[b]
α-Fe_2O_3	LiCl	22	34.0	8.4[m]	5.5	5.7	11.2	−8.3	7.7	80	3.7	2.9	Breeusma (1973)[b]
α-Fe_2O_3	NaCl	22	80.0	8.5[n]	5.5	5.8	11.3	−9.7	7.7	90	2.8	3.2	Liang (1988)[b]
α-Fe_2O_3	KCl	22	29.6	9.5	5.5	6.8	12.3	−10.5	8.0	90	2.6	2.1	Penners et al. (1986)[e]
α-Fe_2O_3	CsCl	22	34.0	8.4[m]	5.5	5.7	11.2	−9.1	7.5	90	2.9	2.7	Breeusma (1973)[b]
α-Fe_2O_3	$NaNO_3$	22	6.36	8.5	5.5	5.8	11.1	−8.9	7.7	190	2.5	2.1	Gunnarsson et al. (2000)[e]
α-Fe_2O_3	$NaNO_3$	22	15.1	9.2	5.5	6.5	12.0	−9.6	8.8	120	2.9	2.9	Schudel et al. (1997)[e]
α-Fe_2O_3	$NaNO_3$	22	16.7	9.0	5.5	6.3	11.8	−9.6	8.2	110	2.7	2.5	Gunnarsson et al. (2001)[e]
α-Fe_2O_3	$NaNO_3$	22	27.4	9.2	5.5	6.5	12.0	−9.9	8.3	115	2.8	2.6	Schudel et al. (1997)[e]
α-Fe_2O_3	$NaNO_3$	22	28.3	9.5[o]	5.5	6.8	12.3	−10.2	8.5	120	2.8	2.5	Christl and Kretzschmar (1999)[e]
α-Fe_2O_3	KNO_3	22	29.0	8.6[p]	5.5	5.9	11.4	−9.4	7.6	95	2.8	2.6	Fokkink (1987)[b]
α-Fe_2O_3	KNO_3	22[f]	32.0	8.5[q]	5.5	5.8	11.3	−8.7	8.0	95	3.4	3.1	Yates (1975)[b]
α-Fe_2O_3	KNO_3	22	32.3	9.1	5.5	6.4	11.9	−9.9	7.2	92	2.8	2.1	Gibb and Koopal (1990)[e]
α-Fe_2O_3	$NaClO_4$	22	21.0	8.4[r]	5.5	5.7	11.1	−8.5	7.9	110	3.3	3.0	Onoda and de Bruyn (1966)[e]
α-Al_2O_3	$NaNO_3$	30.5	12.0	8.9[s]	5.6	6.1	11.7	−9.3	8.2	100	3.0	2.7	Hayes et al. (1991)[c]
γ-Al_2O_3	NaCl	8.0	100.0	8.7	5.9	5.8	11.7	−9.0	8.0	90	3.5	3.2	Huang and Stumm (1973)[b]
γ-Al_2O_3	NaCl	8.0	154.0	8.1	5.9	5.2	11.1	−8.8	7.0	110	3.3	2.9	Sprycha (1989)[b]
α-$Al(OH)_3$	NaCl	10.0	13.0	8.1[t]	5.6	5.3	10.9	−8.9	7.5	40	2.2	2.3	Weerasooriya et al. (2001)[e]
α-$Al(OH)_3$	$NaClO_4$	10.0	3.4	10.0[u]	5.6	7.2	12.8	−10.5[x]	9.7	60	1.9	2.1	McKinley et al. (1995)[e]
α-SiO_2	NaCl	4.8[l]	11.4	2.3	8.4	−1.9	6.5	−4.7	−0.1[y]	60	1.5	1.5	Michael and Williams (1984)[e]

α-SiO_2	NaCl	4.5[l]	4.15	3.0	8.4	−1.2	7.2	−6.5	−0.5[y]	100	0.0	0.0	Riese (1982)[b]
α-SiO_2	KNO_3	11.4	11.57	2.0	8.4	−2.2	6.2	−6.0	−2.0	105	0.3	0.3	Huang (1996)[a]
am. SiO_2	LiCl	4.6	300.0	2.8[v]	8.4	−1.4	7.0	−7.4	−1.8[y]	90	0.7	0.7	Milonji'c (1987)[e]
am. SiO_2	LiCl	4.6	266.0	2.8[v]	8.4	−1.4	7.0	−6.0	−0.4	60	2.1	2.1	Sonnefeld et al. (1995)[e]
am. SiO_2	NaCl	4.6	43.0	2.4	8.4	−1.8	6.6	−5.4	−0.6[y]	67	1.5	1.5	Sonnefeld et al. (2001)[e]
am. SiO_2	NaCl	4.6	180.0	2.8[v]	8.4	−1.4	7.0	−6.9	−1.3[y]	100	1.0	1.0	Bolt (1957)[b]
am. SiO_2	NaCl	4.6	380.0	2.8[v]	8.4	−1.4	7.0	−6.7	−1.1[y]	65	1.5	1.5	Casey (1994)[e]
am. SiO_2	NaCl	4.6	300.0	2.8[v]	8.4	−1.4	7.0	−7.0	−1.4[y]	95	1.1	1.1	Milonji'c (1987)[e]
am. SiO_2	KCl	4.6	170.0	3.0	8.4	−1.2	7.2	−6.4	−0.4[y]	120	1.7	1.7	Abendroth (1970)[b]
am. SiO_2	KCl	4.6	50.0	2.8[v]	8.4	−1.4	7.0	−6.0	−0.4[y]	70	1.4	1.4	Goloub et al. (1996)[e]
am. SiO_2	KCl	4.6	266.0	2.8[v]	8.4	−1.4	7.0	−5.9	−0.3	70	2.2	2.2	Sonnefeld et al. (1995)[e]
am. SiO_2	KNO_3	4.6	359.4	3.2[w]	8.4	−1.0	7.4	−7.2	−0.8[y]	130	1.4	1.4	Csobán and Joó (1999)[e]
am. SiO_2	CsCl	4.6	384.0	2.8[v]	8.4	−1.4	7.0	−6.1	−0.4[y]	95[z]	2.2	2.2	Marmier et al. (1999)[e]
am. SiO_2	$N(CH_3)_4Cl$	4.6	380.0	2.8[v]	8.4	−1.4	7.0	−5.2	0.4[y]	50	3.0	3.0	Casey (1994)[a]

[a] Sverjensky (2001).
[b] Sahai and Sverjensky (1997a).
[c] Criscenti and Sverjensky (1999).
[d] Criscenti and Sverjensky (2002).
[e] Present study (see Appendix).
[f] Tritium exchange experiments.
[g] Point-of-zero-salt effect from Machesky et al. (1998).
[h] Point-of-zero-salt effect from lowest ionic strengths in Figures 9 and 13 (Bérubé, 1967).
[i] Point-of-zero-salt effect from Ali (1994).
[j] Point-of-zero-salt effect from Lumsden and Evans (1994).
[k] Point-of-zero-salt effect for the NaCl in which anion and cation bind almost equally (Villalobos and Leckie, 2001).
[l] Point-of-zero-salt effect from Venema et al. (1996).
[m] Point-of-zero-salt effect from Breeusma (1973).
[n] Point-of-zero-salt effect from Liang (1988).
[o] Point-of-zero-salt effect from Christl and Kretzschmar (1999).
[p] Point-of-zero-salt effect from Fokkink (1987).
[q] Point-of-zero-salt effect from Yates (1975).
[r] Point-of-zero-salt effect from lowest ionic strengths (Onoda and de Bruyn, 1966).
[s] Point-of-zero-salt effect from Hayes et al. (1991).
[t] Point-of-zero-salt effect from lowest ionic strengths (Weerasooriya et al., 2001).
[u] Point-of-zero-salt effect estimated by Hiemstra et al. (1987).
[v] Predicted value from Table 4.
[w] Pers. comm. from Joó.
[x] Estimated based on the zpc and $\log {}^*K^0_{L^-}$.
[y] Estimated based on the zpc and $\log {}^*K^0_{M^+}$.
[z] Predicted value for NaCl solutions from Sverjensky (2001).